INVESTIGATING THE EFFECT OF POROSITY ON THE ELASTOPLASTIC BEHAVIOR OF POWDER-BASED SINTERED METALS THROUGH FINITE ELEMENT ANALYSIS

By © D. Frank Thomas, B.Eng.

A thesis submitted to the

School of Graduate Studies

in partial fulfillment of the requirements of the degree of

Master of Engineering

Memorial University of Newfoundland

October 21st, 2021

St. John's, Newfoundland

Abstract

The effect of porosity, void shape, and aspect ratio on the mechanical behavior of porous ductile metals was studied. Traditional finite element models were developed to predict the elastic modulus and yield stress of porous representative volume elements as a function of porosity and void aspect ratio. Corresponding models were built and tested in ABAQUS for comparison. The effect of void shape and aspect ratio on effective mechanical properties was observed and the necessity of finite element simulations was confirmed. An algorithm for the generation of realistic porous powder-based sintered representative volume element models was fully developed and implemented. A series of models were generated and simulations were performed to extract the effective stress-strain behavior using continuum mechanics methods. Comparisons to existing experimental data for porous sintered metals determined that the three dimensional models generated by the novel algorithm accurately predict the elastic, yield, and plastic deformation behavior of porous sintered metals.

General Summary

The following work details an investigation into the effect of porosity and pore shape on the behavior of porous metals. These porous metals are less dense than expected due to internal pockets of gas or empty space called voids. The total volume of the internal voids, as well as the shape and aspect ratio of these voids, is known to have a pronounced effect on the stiffness and strength of a porous material compared to the fully dense characteristics. The research presented here first demonstrates and confirms the effect of void shape and aspect ratio on the mechanical properties of metals. An algorithm is then developed to generate models of porous material that serve as a more realistic representation of the voids found in 3D printed metals. These new models are found to accurately recreate existing experimental data from actual 3D printed metal specimens.

Acknowledgements

At this time I would like to express my most sincere appreciation and gratitude to those who have supported me throughout this program and indeed throughout the difficult period in which it was completed.

To my supervisor Dr. Sam Nakhla, I am immensely grateful for the time and effort you have devoted to my development both professionally and personally. The relentless motivation and vigor that you pour into each endeavor is a truly aspirational phenomenon. The level of respect which you both command and exude inspires each of your students to strive for greater things than their conception of self would otherwise allow. Your wit, candor, and camaraderie has been tremendously uplifting throughout this trying time. Thank you for constantly elevating those around you and for uncompromisingly pushing your students to achieve the lofty potential that you sense in each of us.

To my parents, Floyd and Jill, who had fought tooth and nail for the first two years of my undergraduate degree to instill the confidence and perseverance I required to succeed. Were it not for your truly inflexible will to see me realize my potential I surely would not have reached for such a satisfying and fulfilling career.

To my best friend and partner Beatrice, I am very thankful to have had you in my corner throughout this chapter of my life. Your consistent encouragement and understanding, love and consideration have made this all possible. I credit your perceptiveness and insistence on self-care to my continuing sanity.

I would also like to thank my friend and colleague Dr. Ahmed Elruby for all of his kindness, support, contributions, and selflessness throughout the course of this pursuit.

Table of Contents

List of Tables

List of Figures

Abbreviations and Symbols

2D	Two-Dimensional
3D	Three-Dimensional
AM	Additive Manufacturing
EBM	Electron Beam Melting
FEA	Finite Element Analysis
PDF	Probability Density Function
RVE	Representative Volume Element
SLM	Selective Laser Melting
SLS	Selective Laser Sintering

Section 1

ρ	Specimen density
ρ_o	Wrought material density
P	Specimen porosity

Section 3

α	Yield offset
ε	Normal strain
σ	Normal stress
λ	Aspect ratio of primary axis lengths
σ_y	Material yield stress
$\sigma_y{}'$	Effective yield stress
a	Void major axis length
b	Void minor axis length
B	First derivate of shape function matrix

E Elastic modulus

k Spring stiffness

L Spring length

n Hardening exponent

N Shape function of non-uniform bar element

Section 4

ν Poisson's ratio

B_i Internal boundary length

B_o External boundary length

c_i Compaction coefficient of model i

D Normal distance from plane of intersection to particle center

err Absolute error in achieved porosity

E Spherical excess

p_i Achieved porosity of model i

P_t Target porosity

R_i Selected particle radius

R_{min} Minimum particle radius

1. Introduction

1.1. Background

Porosity is a physical property of a material which describes the volumetric fraction of a specimen that is effectively void of structurally significant material. For non-composite materials the porosity of a specimen is functionally tied to its relative density by Equation 1.1, where ρ is the specimen density and ρ_o is the established fully-sound material density.

$$P = 1 - \frac{\rho}{\rho_o} \tag{1.1}$$

A material may exhibit a reduced density and therefore an increased porosity through a variety of mechanical, thermal, or chemical routes, the most prominent being induced porosity resulting from fabrication processes such as casting and curing. Porous materials are generally understood to contain a multitude of uniformly distributed voids of various shapes and sizes, however, this designation incorporates everything from cast metals with gas impurities to cellular structures and foams. The voids whose volumetric sum comprises the porosity level have been observed to vary wildly in size and shape depending on the fabrication method and post-processing of the material. Porosity level is known to be inversely related to various mechanical properties including elastic modulus, yield stress, ultimate tensile strength, failure strain, and fatigue strength in metals, and many analytical models have been developed to capture the effect of porosity on these characteristics. A sizeable list of linear, power, and exponential relationships describing the effect of porosity on elastic modulus was tabulated and investigated by Choren et al. in the interest of informing additive manufacturing design [1].

The emergence of additive manufacturing, specifically powder-based metal AM, has drastically increased the prevalence of porous materials with non-traditional void shapes. The voids found in sintered materials are observed to have a degree of variance that is significantly greater than that of non-sintered material voids, as well as more extreme aspect ratios, stress concentrators, and potential void interactions. Given the relative novelty and rise in popularity it is necessary to investigate the relationship between porosity and mechanical behavior for these materials.

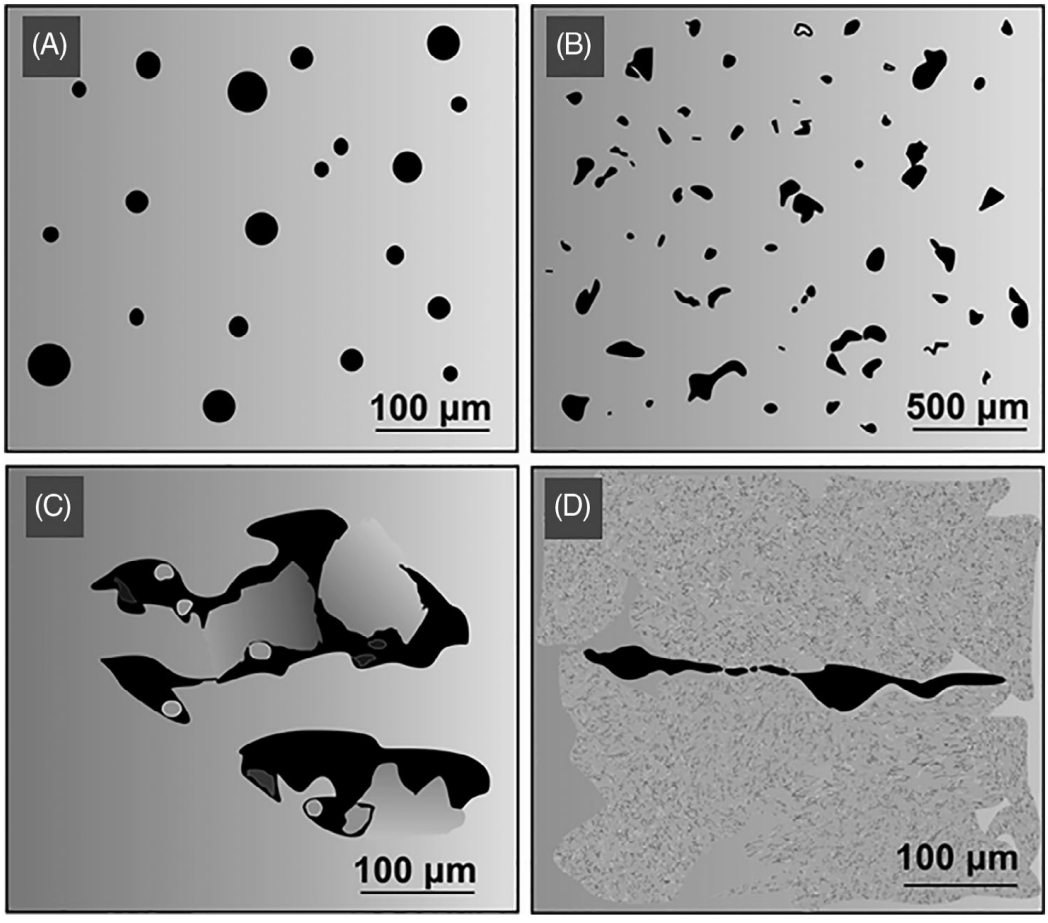

Figure 1: Characteristic Pores in Laser-Based Powder Bed Fusion Parts [2]

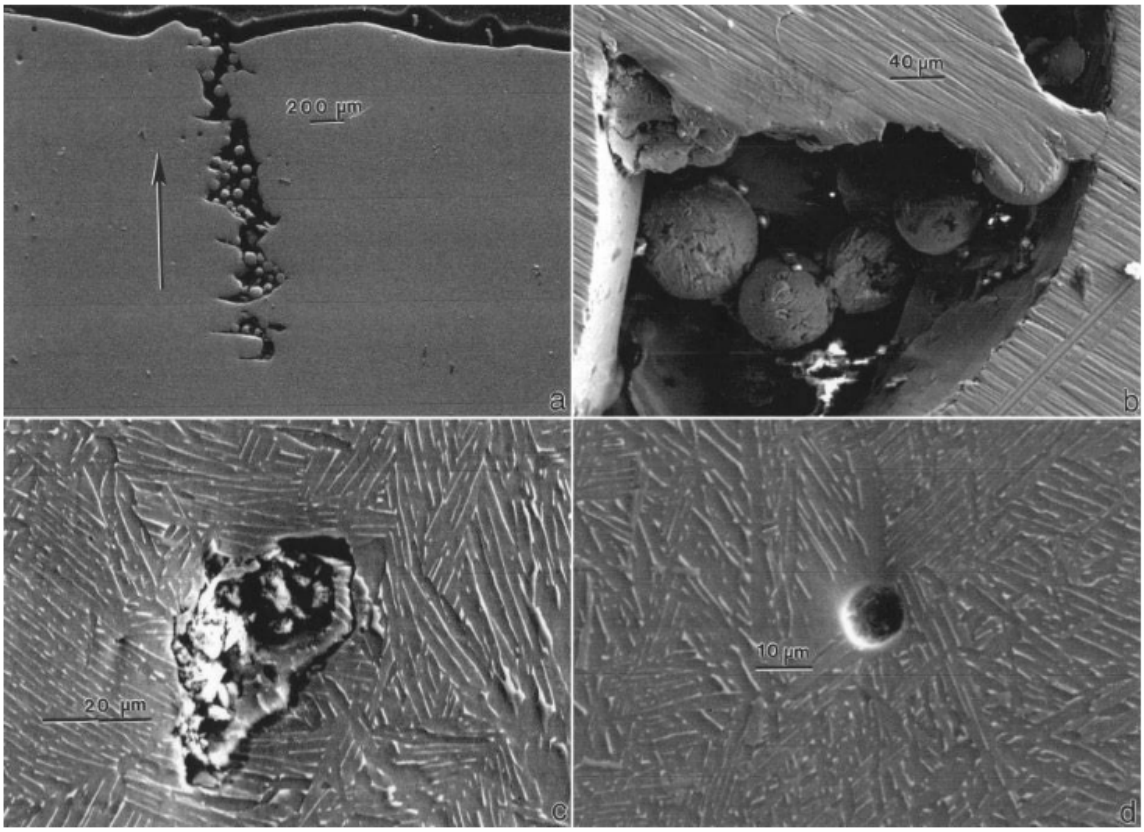

Figure 2: Examples of Void Defects in Non-Optimized EBM Builds with Cylindrical Geometries from Ti-6Al-4V Powder [3]

1.2. Thesis Overview

The purpose of this thesis was to investigate the effect of porosity on the mechanical behavior of porous metals fabricated from a powdered base material by process of sintering, specifically the additive manufacturing process of selective laser sintering. The investigations conducted include traditional finite element analysis of single-void models, finite element analysis simulations of single-void representative volume element models, and the development and testing of an algorithm designed to replicate particle mechanics and generate realistic models of porous sintered materials for the purpose of finite element simulation. Throughout the course of these investigations the effect of porosity, void shape, and void shape characteristics were tested to

determine their effect on material behavior. A series of finite element simulations which correspond to existing experimental data were conducted using models generated by the novel algorithm to gauge the accuracy of the realistic particle-based models.

Section 2 presents a literature review and general overview of the concepts and physical phenomena investigated in this work. Section 3 examines the behavior of porous materials modelled as units with single void inclusions. In this section, traditional finite element methods are employed to develop equations that describe the behavior of these single void models. The performance of these analytical models is tested against computer simulated models to ascertain the significance of non-linear deformations in porous materials and validate further simulations. Section 4 outlines the development of a novel algorithm for the generation of microstructural models of porous particle-based solids. Section 5 is comprised of the testing and analysis performed to verify and validate the algorithm developed in Section 4.

1.3. Co-authorship Statement

The work presented in this thesis has been the result of the collaborative efforts of the author Mr. D. Frank Thomas [DFT], program supervisor Dr. Sam Nakhla [SN], and Dr. Ahmed Elruby [AE]. This co-authorship statement adheres to the format put forth by Elsevier's CRediT (Contributor Roles Taxonomy) author statement guidelines.

Co-authorship credit for each facet of this work is as follows:

Conceptualization [SN, DFT, AE]. Methodology [DFT, AE, SN]. Software [DFT, AE]. Validation [DFT, AE, SN]. Formal analysis [DFT, AE]. Investigation [DFT, AE, SN]. Resources [SN]. Data curation [DFT, AE]. Writing - original draft [DFT]. Writing - review & editing [DFT, AE, SN]. Visualization [DFT, AE]. Supervision [SN]. Project administration [AE, SN]. Funding acquisition [SN].

1.4. Publication Status

The material presented in Section 4 and Section 5 was partially presented in the conference proceedings of the 2021 CSME International Congress. This material also comprises an article which is in a final review stage for submission to the journal Additive Manufacturing at the time of thesis submission.

2. Literature Review

The goal of metal and ceramic-based additive manufacturing (AM) is to fabricate complex, near net shape parts rapidly and with minimal tooling cost [4–6]. Selective laser sintering (SLS) and selective laser melting (SLM) are two subtly distinct methods of powder-based AM. Powder-based AM fabricate near-net shape parts primarily via one of two methods: powder bed systems, which selectively heat consecutive cross-sections with a controlled laser, and powder feed systems which simultaneously heat and deposit material from a moving head [7,8]. The SLM process is characterized by the complete melting and solidification of powder base materials during fabrication. By contrast, the SLS process heats particles to a temperature below the melting point but sufficiently high as to promote the fusion of neighboring particles through solid-state sintering. Materials produced via SLS are observed to have a macrostructure similar to sintered compacts produced via powder metallurgy (PM) processes. Powder-based sintered metals are observed to have decreased grain size compared to the wrought material and mechanical properties that are distinct from that of SLM and non-AM material [8–10]. Research from Iebba et al. [11] and a recent investigation by Brika et al. [12] indicates a link between the morphology and size distribution of powder base particles and the mechanical behavior of corresponding 3D printed materials.

The naturally occurring void imperfections observed in sintered materials are unique in both shape and size compared to the macro-scale voids observed in non-sintered solids, which are generally ellipsoidal. This shape disparity has a significant effect on the material's mechanical behaviour [13]. Specifically, void shapes inherent in sintered materials facilitate compaction deformation under compressive loading thereby exacerbating the disparity between the tensile and compressive elastoplastic behavior of sintered metals [14,15]. The accurate prediction of the

mechanical properties of low porosity sintered materials is essential to the process of powder-based AM design.

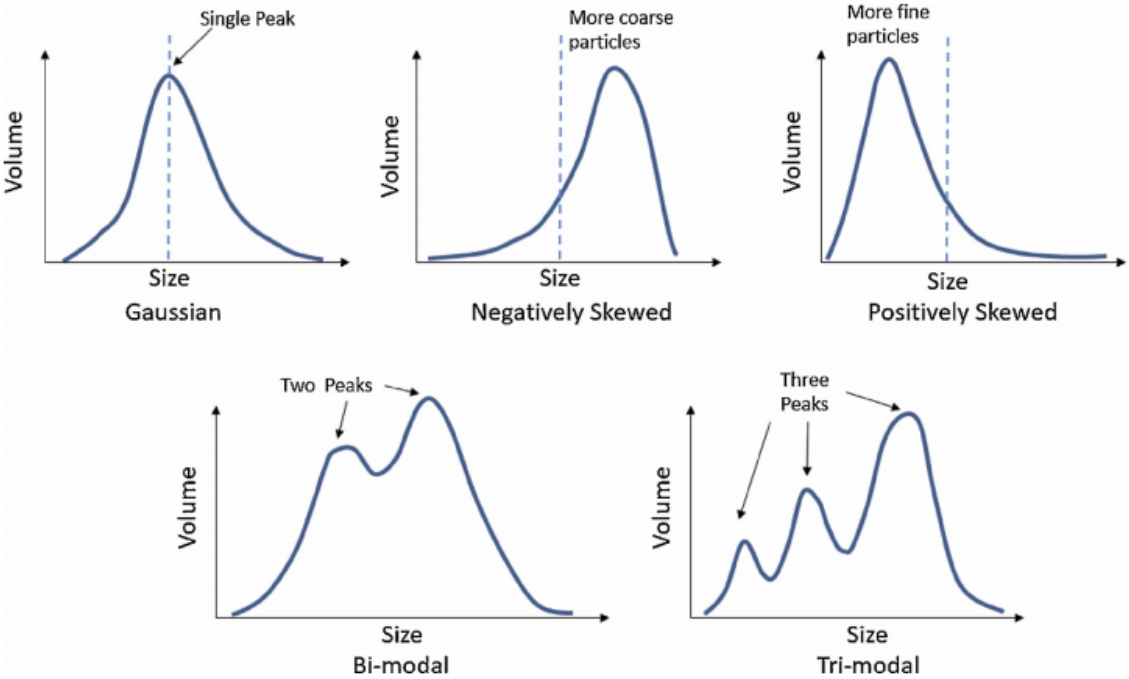

Figure 3: Particle Size Distribution PDFs

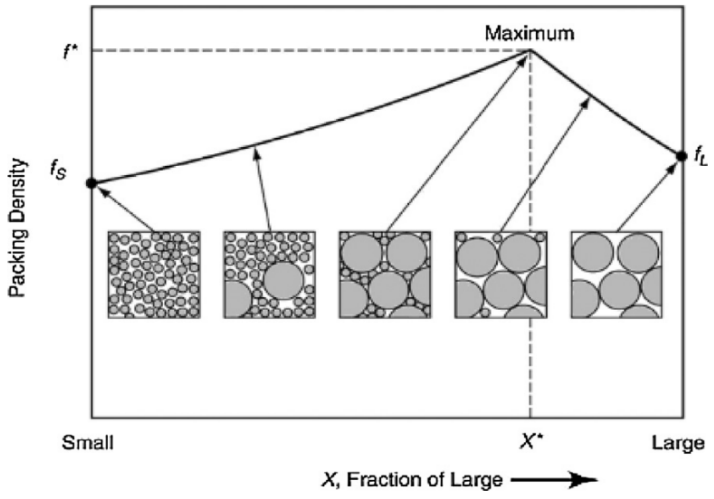

Figure 4: Packing Density Plot for Bi-Modal Particle Size Distribution

Investigations into the mechanical behavior of AM materials have been augmented significantly by simulation techniques developed through composite materials research, such as the representative volume element (RVE), in concert with modern finite element analysis (FEA) [16,17]. Microstructure modelling in particular has proven to be a powerful tool for assessing material properties [18]. Modelling and analysis of a microstructural element can accurately predict behavior while simplifying the process of parameterization where a descriptive analytical model is desired. In the case of porous sintered materials, the microstructure has yet to be modelled in a generalized manner such that behavior is accurately predicted [19]. For the purposes of simulating a sintered material we have chosen two essential physical measurements: a probability distribution function (PDF) of particle radii and the relative density of the finished part. These parameters are chosen prior to manufacturing, where the relative density of a completed part is determined experimentally or is, in some cases, reported as a function of scan speed, temperature, pressure, and/or laser power [20,21].

The precise manner of computational solution we have developed is an investigation of the homogenized response of a porous sintered material. This entails constructing a pseudo-random, geometrically analogous micro- or meso-structure whose mechanical behaviour is equivalent to that of physical specimens. Homogenization and generalization of stress-strain behaviour from microstructural simulation is made possible by the application of continuum mechanics principles. This information is sufficient to evaluate the mechanical behaviour of an arbitrary shape whose material properties are known. The continuum approach introduces the assumption that the structural element may be treated as an infinitesimally small element surrounded by identical cells under identical load conditions. The use of cubic periodic elements for the purposes of investigating effective mechanical properties has been validated for porous, powder-based AM

metals [22–24]. In addition to vastly simplifying microstructure simulations as a whole, the cost-effective simulation of infinite cells has been a powerful tool for those studying porous and cellular solids.

One of the earliest instances of the attempted simulation of porous solids comes from Woodmansee [25], who attempted to categorize the response of porous materials by porosity. This work was unable to evaluate the behaviour of non-linear materials. From there a variety of non-random porous and cellular models cropped up for use in particle-reinforced ceramics and the investigation of porous material behaviour [26]. The microstructure modelling toolkit Mote3D provides tools primarily for the generation of particle-reinforced composite models with support for sintered particle modelling, however it does not consider relative density as a parameter, instead modelling sintered particles based on sinter neck distance [27]. This method is not appropriate for the modelling of sintered AM microstructures as mechanical properties are very sensitive to changes in relative density induced by void defects [28,29] and powder morphology [30]. It is therefore imperative that a sintered powder model achieve a precise targeted relative density.

3. Pore Shape Effect

To study the effect of void shape and void aspect ratio on the mechanical behavior of a porous material, a series of finite element analysis simulations were conducted on 3 primary shapes at the same fractional porosity level in 2D and 3D. The 2D void shapes used in this study are elliptical, rectangular, and equilateral quadrilateral. In 3D the void shapes are ellipsoidal, cuboidal, and equilateral octahedral. The aspect ratio refers to the ratio of the primary axis length (in the direction of applied load) to the secondary axis length. In 3D the aspect ratio defines both the 1-2 and the 1-3 axis length ratios. The aspect ratios studied in these simulations are 1:2, 2:3, 1:1, 3:2, and 2:1 at a porosity of 4%.

The models containing ellipsoidal voids are intended to capture the behavior expected to arise from traditionally manufactured porous materials, such as cast metals or resins. These voids are generally a result of thermal effects, impurities, or trapped gasses. The quadrilateral/octahedral void models represent materials which contain significant stress concentrators aligned normal to the direction of applied force, which is akin to the voids we observe in powder-based sintered and additive manufactured metals and ceramics. Lastly the rectangular voids show the mechanical behavior of a porous material with stress concentrating features that are not explicitly oriented in the worst-case configuration, as the quadrilateral voids are.

3.1. Analytical Modelling

For each of the void shapes, a traditional finite element model was derived to predict the effective stiffness and yield stress of the porous material. A unit element containing a void located at the center is used to formulate a system of springs in parallel as seen in Figure 5. The axial

stiffness of each individual segment is derived by integration through the direction of applied load, otherwise known as the analytical stiffness method for a non-uniform bar.

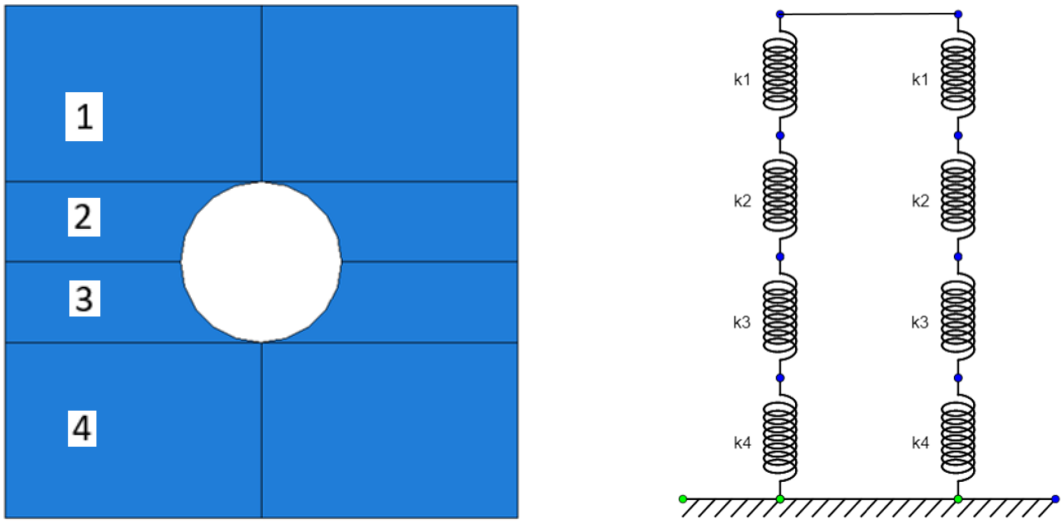

Figure 5: Model & Spring Diagram

It can be shown that for the above spring diagram, where $k_1 = k_4$ and $k_2 = k_3$ the total stiffness of the system is:

$$k_{tot} = \frac{k_1 k_2}{k_1 + k_2} \tag{3.1}$$

Given that the length L_1 is a known quantity defined by the porosity and aspect ratio for each shape, the stiffness k_1 is derived below in matrix form.

$$\underline{k_1} = \int_0^{L_1} \underline{B}^T \underline{D}\, \underline{B} A \, dx = \frac{E}{2L_1^2}\begin{bmatrix} 1 & -1 \\ -1 & 1 \end{bmatrix} \int_0^{L_1} 1 \, dx$$

$$\underline{k_1} = \frac{E}{2L_1}\begin{bmatrix} 1 & -1 \\ -1 & 1 \end{bmatrix} = \frac{E}{2\left(\frac{1}{2} - a\right)}\begin{bmatrix} 1 & -1 \\ -1 & 1 \end{bmatrix} = \frac{\boldsymbol{E}}{\boldsymbol{1 - 2a}}\begin{bmatrix} \mathbf{1} & \mathbf{-1} \\ \mathbf{-1} & \mathbf{1} \end{bmatrix} \tag{3.2}$$

Where a is the major axis length of the void. The B matrix is derived as follows, assuming linear displacement under fully elastic strain and using shape functions N_1 and N_2 as shown.

$$u(x) = N_1 d_1 + N_2 d_2 \tag{3.3}$$

$$N_1 = 1 - \frac{x}{L_1} \tag{3.4}$$

$$N_2 = \frac{x}{L_1} \tag{3.5}$$

$$\underline{B} = \underline{N}' = \frac{1}{L_1}[L_1 - x \quad x]\frac{d}{dx} = \frac{1}{L_1}[-1 \quad 1] \tag{3.6}$$

Unlike the derivation from Equation 3.2, the stiffness equation for k_2 considers a case where the derivate of area with respect to x is non-zero. The function $A(x)$ varies for each void shape. The following section details the derivation of the various model characteristics.

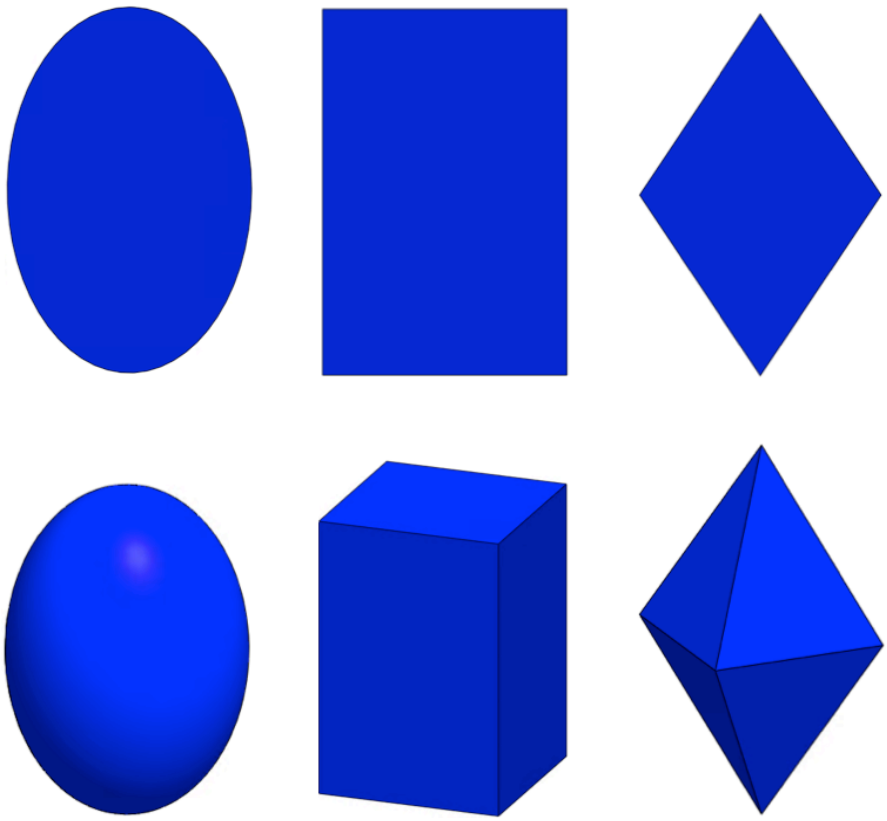

Figure 6: Void Shapes at 3:2 Aspect Ratio

3.1.1. Elliptical Void Stiffness Derivation

A regular ellipse is described by the equation $\left(\frac{x}{a}\right)^2 + \left(\frac{y}{b}\right)^2 = 1$ where a and b are the major and minor axis lengths respectively. The area of an ellipse is given by $A = \pi ab$ and the aspect ratio gives the equation $\lambda = a/b$. Since the enclosing region is a unit square, the area of the void is exactly equal to the porosity P of the material. Given some porosity and aspect ratio the corresponding axis lengths are developed as follows.

$$P = \pi ab \tag{3.7}$$

$$\lambda = \frac{a}{b} \rightarrow b = \frac{a}{\lambda} \tag{3.8}$$

$$P = \pi a\left(\frac{a}{\lambda}\right) \rightarrow a = \sqrt{\frac{\lambda P}{\pi}} \tag{3.9}$$

Where a is both the primary axis length and the length of element 2.

$$b = \frac{a}{\lambda} = \sqrt{\frac{P}{\lambda\pi}} \tag{3.10}$$

$$A_{min} = 1 - 2b = 1 - 2\sqrt{\frac{P}{\lambda\pi}} \tag{3.11}$$

Length of element 1:

$$L_1 = \frac{1}{2} - \sqrt{\frac{\lambda P}{\pi}} \tag{3.12}$$

Stiffness of element 1:

$$k_1 = \frac{EA_1}{L_1} = \frac{\boldsymbol{E}}{\left(\mathbf{1} - \mathbf{2}\sqrt{\frac{\boldsymbol{\lambda P}}{\boldsymbol{\pi}}}\right)} \tag{3.13}$$

Stiffness of element 2:

$$k_2 = \frac{E}{L_2^2}\int_0^{L_2} A_2(x)\,dx \tag{3.14}$$

Rearranging the equation of an ellipse gives y, the width of the void, as a function of x:

$$y = b\sqrt{1 - \left(\frac{x}{a}\right)^2} \tag{3.15}$$

Area of solid section as a function of x:

$$A_2(x) = 0.5 - b\sqrt{1 - \left(\frac{x}{a}\right)^2} \tag{3.16}$$

We know that in Equation 3.14 the length L_2 is equal to a. Substituting 3.16 into 3.14:

$$k_2 = \frac{E}{a^2}\int_0^a 0.5 - b\sqrt{1 - \left(\frac{x}{a}\right)^2}\,dx$$

$$k_2 = \frac{E}{a^2}\left[\frac{1}{2}x - \frac{1}{2}bx\sqrt{1 - \left(\frac{x}{a}\right)^2} - \frac{1}{2}ab\,\mathrm{atan}\left(\frac{x}{a\sqrt{1 - \left(\frac{x}{a}\right)^2}}\right)\right]_0^a \tag{3.17}$$

At $x = 0$ the integration term is zero. At $x \to a$ the term $\sqrt{1 - \left(\frac{x}{a}\right)^2}$ approaches zero and the arctangent term consequently approaches $\frac{\pi}{2}$. The simplified equation is therefore:

$$k_2 = \frac{E}{a^2}\left(\frac{1}{2}a - \frac{1}{4}ab\pi\right) \tag{3.18}$$

Substituting Equations 3.7 and 3.9 into 3.18:

$$k_2 = \frac{E\pi}{4\lambda P}\left(2\sqrt{\frac{\lambda P}{\pi}} - P\right) = \frac{\boldsymbol{E\pi}}{\boldsymbol{4\lambda}}\left(\sqrt{\frac{\boldsymbol{4\lambda}}{\boldsymbol{\pi P}}} - \mathbf{1}\right) \tag{3.19}$$

The total stiffness can be written as follows:

$$k_{tot} = \frac{E\left(2\sqrt{\pi\lambda} - \pi\sqrt{P}\right)}{2\sqrt{\pi\lambda} - \pi\sqrt{P} + 2P\sqrt{\pi\lambda}} \tag{3.20}$$

The effective yield stress of the analytical model is approximated as the overall stress at which yield should occur at the weakest cross-section of the model, i.e. the smallest area. The effective yield of the unit element model is therefore a function of the material yield stress multiplied by a geometric function of porosity an aspect ratio describing the width at the midpoint.

Effective yield stress equation for a 2D elliptical void:

$$\sigma_y' = \sigma_y\left(1 - 2\sqrt{\frac{P}{\lambda\pi}}\right) \tag{3.21}$$

3.1.2. Rectangular Void Stiffness Derivation

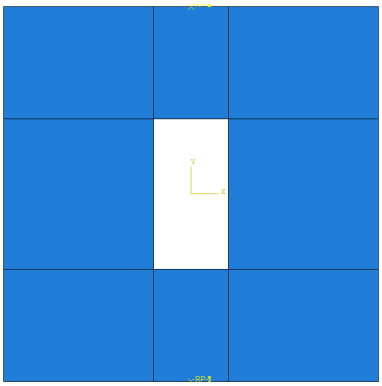

Figure 7: Rectangular Void Model (2:1 Aspect Ratio)

$$P = 4ab \rightarrow \quad a = \frac{1}{2}\sqrt{\lambda P} \tag{3.22}$$

$$b = \frac{1}{2}\sqrt{\frac{P}{\lambda}} \tag{3.23}$$

$$A_{min} = 1 - \sqrt{\frac{P}{\lambda}} \tag{3.24}$$

Length of element 1:

$$L_1 = \frac{1}{2}\left(1 - \sqrt{\lambda P}\right) \tag{3.25}$$

Stiffness of element 1:

$$k_1 = \frac{EA_1}{L_1} = \frac{\boldsymbol{E}}{\left(\boldsymbol{1 - \sqrt{\lambda P}}\right)} \tag{3.26}$$

Stiffness of element 2:

$$A_2(x) = 0.5 - b = \frac{1}{2}\left(1 - \sqrt{\frac{P}{\lambda}}\right) \tag{3.27}$$

$$k_2 = \frac{E}{2a^2}\int_0^a \left(1 - \sqrt{\frac{P}{\lambda}}\right) dx = \frac{E}{2a}\left(1 - \sqrt{\frac{P}{\lambda}}\right)$$

$$k_2 = \frac{E}{\sqrt{\lambda P}} * \frac{\left(\sqrt{\lambda} - \sqrt{P}\right)}{\sqrt{\lambda}} = \frac{\boldsymbol{E}}{\boldsymbol{\lambda}}\left(\sqrt{\frac{\boldsymbol{\lambda}}{\boldsymbol{P}}} - \mathbf{1}\right) \tag{3.28}$$

Total stiffness:

$$k_{tot} = \frac{E\left(\sqrt{P\lambda} - \lambda\right)}{\sqrt{P\lambda} - \lambda - P\lambda} \tag{3.29}$$

Effective yield stress:

$$\sigma_y' = \sigma_y\left(1 - \sqrt{\frac{P}{\lambda}}\right) \tag{3.30}$$

3.1.3. Quadrilateral Void Stiffness Derivation

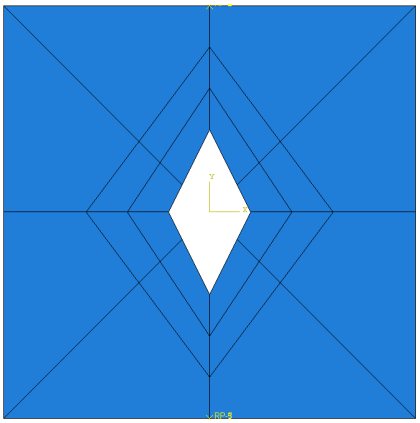

Figure 8: Quadrilateral Void Model (2:1 Aspect Ratio)

$$P = 2ab \rightarrow \quad a = \sqrt{\frac{P\lambda}{2}} \tag{3.31}$$

$$b = \sqrt{\frac{P}{2\lambda}} \tag{3.32}$$

$$A_{min} = 1 - 2b = 1 - \sqrt{\frac{2P}{\lambda}} \tag{3.33}$$

Element 1

$$L_1 = \frac{1}{2} - a = \frac{1}{2}\left(1 - \sqrt{2P\lambda}\right) \tag{3.34}$$

$$k_1 = \frac{EA_1}{L_1} = \frac{\boldsymbol{E}}{\boldsymbol{1 - \sqrt{2P\lambda}}} \tag{3.35}$$

Element 2

$$A_2(x) = 0.5 - b\left(\frac{x}{a}\right) \tag{3.36}$$

$$k_2 = \frac{E}{a^2}\int_0^a \left(\frac{1}{2} - x\left(\frac{b}{a}\right)\right)dx = \frac{E}{a^2}\left[\frac{1}{2}x - \frac{b}{2a}x^2\right]_0^a$$

$$k_2 = \frac{E}{a^2}\left(\frac{1}{2}a - \frac{1}{2}ab\right) = \boldsymbol{E}\left(\frac{\boldsymbol{\sqrt{2\lambda} - \sqrt{P}}}{\boldsymbol{2\lambda\sqrt{P}}}\right) \tag{3.37}$$

Total stiffness:

$$k_{tot} = \frac{E\left(\sqrt{2P\lambda} - 2\lambda\right)}{\sqrt{2P\lambda} - 2\lambda - 2P\lambda} \tag{3.38}$$

Effective yield stress:

$$\sigma_y' = \sigma_y\left(1 - \sqrt{\frac{2P}{\lambda}}\right) \tag{3.39}$$

3.1.4. Ellipsoidal Void Stiffness Derivation

An ellipsoid in 3D is defined by the equation $\left(\frac{x}{a}\right)^2 + \left(\frac{y}{b}\right)^2 + \left(\frac{z}{c}\right)^2 = 1$, where a, b, c are the three primary axis lengths. In this investigation the ellipsoids are modelled as rotationally symmetric about the x-axis, i.e. $b = c$ and any cross-section of the ellipsoid in the y-z plane produces a circle of a well-defined radius. The area of this circle is subtracted from the area of the solid section to give the area function $A_2(x)$ for determining stiffness.

$$P = \frac{4}{3}\pi abc = \frac{4}{3}\pi ab^2 = \frac{4\pi a^3}{3\lambda^2} \tag{3.40}$$

$$a = \left(\frac{3P\lambda^2}{4\pi}\right)^{\frac{1}{3}} \rightarrow \quad b = \left(\frac{3P}{4\pi\lambda}\right)^{\frac{1}{3}} \tag{3.41}$$

$$A_{min} = 1 - \pi b^2 = 1 - \frac{1}{2}\sqrt[3]{\frac{9P^2\pi}{2\lambda^2}} \tag{3.42}$$

Element 1:

$$L_1 = \frac{1}{2} - \left(\frac{3P\lambda^2}{4\pi}\right)^{\frac{1}{3}} \tag{3.43}$$

$$k_1 = \frac{EA_1}{L_1} = \frac{2E}{1 - \left(\frac{6P\lambda^2}{\pi}\right)^{\frac{1}{3}}} = \frac{\boldsymbol{2E\sqrt[3]{\pi}}}{\boldsymbol{\sqrt[3]{\pi} - \sqrt[3]{6P\lambda^2}}} \tag{3.44}$$

Element 2:

$$\left(\frac{x}{a}\right)^2 + \left(\frac{y}{b}\right)^2 + \left(\frac{z}{c}\right)^2 = \left(\frac{x}{a}\right)^2 + 2\left(\frac{y}{b}\right)^2 = 1 \rightarrow \ y = b\sqrt{\frac{1}{2}\left(1 - \left(\frac{x}{a}\right)^2\right)} \tag{3.45}$$

In the context of the cross-section, y is the radius of the circle therefore

$$A_2(x) = 1 - \pi r^2 = 1 - \pi b^2\left(\frac{1}{2}\left(1 - \left(\frac{x}{a}\right)^2\right)\right)$$

$$A_2(x) = 1 - \frac{1}{8}\sqrt[3]{\frac{36\pi P^2}{\lambda^2}} + \frac{\pi}{2\lambda^2}x^2 \tag{3.46}$$

Note: Equation 5.6 is the area of the entire cross-section, unlike the 2D formulations. The resultant stiffness will consequently be modeled as four springs connected in series.

$$k_2 = \frac{E}{a^2}\int_0^a 1 - \frac{1}{8}\sqrt[3]{\frac{36\pi P^2}{\lambda^2}} + \frac{\pi}{2\lambda^2}x^2 \ dx$$

$$k_2 = \frac{E}{a^2}\left[x - \frac{x}{8}\sqrt[3]{\frac{36\pi P^2}{\lambda^2}} + \frac{\pi}{6\lambda^2}x^3\right]_0^a = \boldsymbol{E}\left[\sqrt[3]{\frac{\boldsymbol{4\pi}}{\boldsymbol{3\lambda^2 P}}} - \sqrt[3]{\frac{\boldsymbol{\pi^2 P}}{\boldsymbol{36\lambda^4}}}\right] \tag{3.47}$$

The total stiffness is developed as follows:

$$k_{tot}^{-1} = \frac{2}{k_1} + \frac{2}{k_2} \rightarrow \quad k_{tot} = \frac{1}{2}\frac{k_1 k_2}{k_1 + k_2} \tag{3.48}$$

For an ellipsoidal void:

$$k_{tot} = \frac{E\left(\sqrt[3]{48\lambda^2} - \sqrt[3]{\pi P^2}\right)}{\sqrt[3]{48\lambda^2} - \sqrt[3]{\pi P^2} + P\sqrt[3]{6\lambda^2}} \tag{3.49}$$

Effective yield stress:

$$\sigma_y' = \sigma_y\left(1 - \frac{1}{2}\sqrt[3]{\frac{9P^2\pi}{2\lambda^2}}\right) \tag{3.50}$$

3.1.5. Rectangular Prism Void Stiffness Derivation

The 3D rectangular prismatic void used in this study has side lengths $[2a, 2b, 2b]$ and a volume of $8ab^2$.

$$P = 8ab^2 = \frac{8a^3}{\lambda^2} \rightarrow \quad a = \frac{1}{2}\sqrt[3]{P\lambda^2} \tag{3.51}$$

$$b = \frac{1}{2}\sqrt[3]{\frac{P}{\lambda}} \tag{3.52}$$

$$A_{min} = 1 - (2b)^2 = 1 - \left(\frac{P}{\lambda}\right)^{\frac{2}{3}} \tag{3.53}$$

Element 1:

$$L_1 = \frac{1}{2} - a = \frac{1}{2}\left(1 - \sqrt[3]{P\lambda^2}\right) \tag{3.54}$$

$$k_1 = \frac{EA_1}{L_1} = \frac{\boldsymbol{2E}}{\boldsymbol{1 - \sqrt[3]{P\lambda^2}}} \tag{3.55}$$

Element 2:

$$A_2(x) = 1 - (2b)^2 = 1 - \left(\frac{P}{\lambda}\right)^{\frac{2}{3}} \tag{3.56}$$

Since $A_2(x)$ is constant the stiffness of element 2 is developed as follows:

$$k_2 = \frac{EA_2}{L_2} = \frac{E\left(1 - \left(\frac{P}{\lambda}\right)^{\frac{2}{3}}\right)}{a} = \frac{\boldsymbol{2E\left(1 - \left(\frac{P}{\lambda}\right)^{\frac{2}{3}}\right)}}{\boldsymbol{\sqrt[3]{P\lambda^2}}} \tag{3.57}$$

Effective stiffness (per Equation 5.8):

$$k_{tot} = \frac{E\left(\sqrt[3]{\lambda P^2} - \lambda\right)}{\sqrt[3]{\lambda P^2} - \lambda - \lambda P} \tag{3.58}$$

Effective yield stress:

$$\sigma_y' = \sigma_y\left(1 - \left(\frac{P}{\lambda}\right)^{\frac{2}{3}}\right) \tag{3.59}$$

3.1.6. Octahedral Void Stiffness Derivation

The 3D version of the quadrilateral void shape from 2D is that of an equilateral octahedron, or square bipyramid, where the major and minor axis lengths are the distances between opposing vertices.

The volume of a square bipyramid:

$$V = P = \frac{4}{3}ab^2 = \frac{4a^3}{3\lambda^2} \tag{3.60}$$

$$a = \sqrt[3]{\frac{3\lambda^2 P}{4}} \rightarrow b = \frac{a}{\lambda} = \sqrt[3]{\frac{3P}{4\lambda}} \tag{3.61}$$

$$A_{min} = 1 - 4\left(\frac{1}{2}b^2\right) = 1 - \sqrt[3]{\frac{9P^2}{2\lambda^2}} \tag{3.62}$$

Element 1:

$$L_1 = \frac{1}{2} - a = \frac{1}{2} - \sqrt[3]{\frac{3\lambda^2 P}{4}} \tag{3.63}$$

$$k_1 = \frac{EA_1}{L_1} = \frac{2E}{1 - \sqrt[3]{6\lambda^2 P}} \tag{3.64}$$

A cross-sectional view of this void in the y-z plane presents a square for which the distance from each vertex to the center is equal to some function $y(x)$. Since the points lie on a straight line we develop the following:

$$y(x) = c_1 x + c_2 \tag{3.65}$$

$$y(0) = 0 \rightarrow \ \boldsymbol{c_2 = 0} \tag{3.66}$$

$$y(a) = c_1 a = b \rightarrow \ \boldsymbol{c_1 = \frac{b}{a}} \tag{3.67}$$

The solid area of the cross-section:

$$A_2(x) = 1 - 2y(x)^2 = 1 - 2\left(\frac{b}{a}\right)^2 x^2 = \boldsymbol{1 - 2\left(\frac{x}{\lambda}\right)^2} \tag{3.68}$$

$$k_2 = \frac{E}{a^2}\int_0^a 1 - \frac{2}{\lambda^2}x^2 dx = \frac{E}{a^2}\left[x - \frac{2}{3\lambda^2}x^3\right]_0^a = \frac{\boldsymbol{E\left(\sqrt[3]{12\lambda^2} - \sqrt[3]{2P^2}\right)}}{\boldsymbol{\lambda\sqrt[3]{9P\lambda}}} \tag{3.69}$$

Effective stiffness:

$$k_{tot} = \frac{E\left(\sqrt[3]{6\lambda^2} - \sqrt[3]{P^2}\right)}{\sqrt[3]{6\lambda^2} - \sqrt[3]{P^2} + \sqrt[3]{6P\lambda^2}} \tag{3.70}$$

Effective yield stress:

$$\sigma_y' = \sigma_y\left(1 - \sqrt[3]{\frac{9P^2}{2\lambda^2}}\right) \tag{3.71}$$

3.2. Finite Element Analysis

Computational models were constructed for each void shape for finite element analysis in ABAQUS. For each unique shape a cell partitioning method was implemented to divide the models such that the whole model can be meshed using structured quadrilateral elements (CPS4R) in 2D and structured linear brick elements (C3D8R) in 3D.

To extract the effective mechanical behavior of a porous material from a single unit cell, reference points are placed at the center of the top and bottom faces. A constraint is applied to these faces which ensures that the face nodes experience no translation whatsoever relative to their respective reference points. The bottom reference point is fully fixed with zero degrees of freedom and the top reference point is constrained to only allow for translation in the direction of applied force. A displacement is applied to the top reference point with a ramp function which spans the simulation step. Output requests for force and displacement are applied to the bottom and top nodes respectively. Due to the height and cross-sectional area of the model both being equal to 1, the raw

data collected from these nodes corresponds exactly to the effective stress and strain behavior of the porous representative volume element model.

The model used to define the behavior of the non-porous material is called the deformation plasticity model in ABAQUS, which is based on the Ramberg-Osgood relationship shown in Equation 3.72. This model uses a yield offset constant and a hardening exponent to accurately describe the elastic, yield, and plastic deformation behavior of ductile metals up to the ultimate tensile stress.

$$\varepsilon = \frac{\sigma}{E} + \alpha\sigma\left(\frac{\sigma}{\sigma_y}\right)^{n-1} \tag{3.72}$$

Once simulations are complete, the resultant datasets are analyzed to determine the elastic modulus and yield stress of the representative volume element model and consequently the expected characteristics of the porous material. The yield stress is computed using the yield offset method with the given value α as the offset strain. Linear interpolation is used at the point of intersection to provide a more precise yield stress.

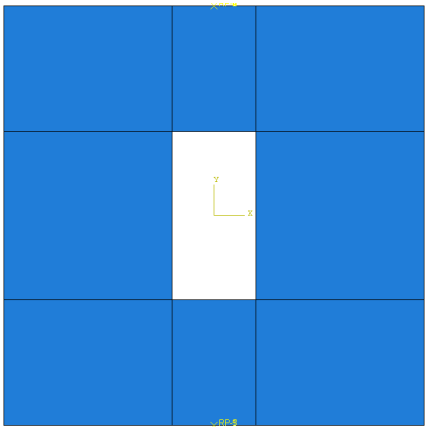

Figure 9: Rectangular Void at 2:1 AR

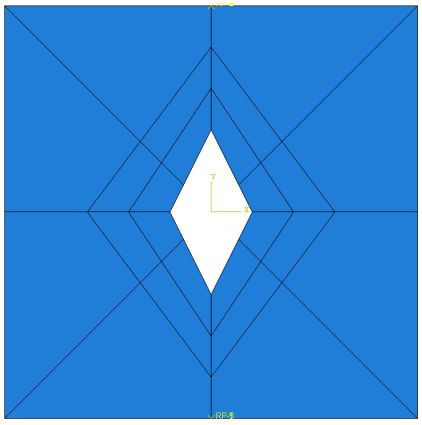

Figure 10: Quadrilateral Void at 2:1 AR

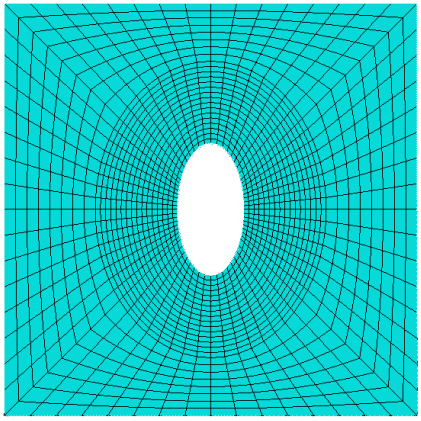

Figure 11: Meshed Elliptical Void at 2:1 AR

3.3. Results & Comparisons

The following tables illustrate the results of the analytical modelling from Section 3.1 and the finite element analysis results for a 4% porous specimen of low strength steel with an elastic modulus of 200 GPa and a yield stress of 500 MPa.

Table 1: 2D Elliptical Void Results

	Elastic Modulus			**Yield Stress**		
Aspect Ratio	Theoretical	Simulated	Difference	Theoretical	Simulated	Difference
2.00	191.3E+9	187.8E+9	1.84%	420.2E+6	445.0E+6	-5.56%
1.50	191.1E+9	185.0E+9	3.28%	407.9E+6	434.2E+6	-6.07%
1.00	190.7E+9	179.6E+9	6.18%	387.2E+6	415.5E+6	-6.81%
0.67	190.3E+9	172.1E+9	10.57%	361.8E+6	391.8E+6	-7.65%
0.50	189.9E+9	165.1E+9	15.00%	340.4E+6	371.5E+6	-8.38%

Table 2: 2D Rectangular Void Results

	Elastic Modulus			**Yield Stress**		
Aspect Ratio	Theoretical	Simulated	Difference	Theoretical	Simulated	Difference
2.00	191.1E+9	186.7E+9	2.36%	429.3E+6	445.3E+6	-3.59%
1.50	190.9E+9	184.1E+9	3.66%	418.4E+6	435.6E+6	-3.97%
1.00	190.5E+9	179.4E+9	6.17%	400.0E+6	419.1E+6	-4.57%
0.67	189.9E+9	172.9E+9	9.84%	377.5E+6	398.5E+6	-5.25%
0.50	189.4E+9	167.0E+9	13.47%	358.6E+6	380.7E+6	-5.82%

Table 3: 2D Quadrilateral Void Results

	Elastic Modulus			Yield Stress		
Aspect Ratio	Theoretical	Simulated	Difference	Theoretical	Simulated	Difference
2.00	191.5E+9	185.4E+9	3.27%	400.0E+6	431.7E+6	-7.34%
1.50	191.3E+9	181.0E+9	5.71%	384.5E+6	416.1E+6	-7.59%
1.00	191.1E+9	172.6E+9	10.75%	358.6E+6	390.5E+6	-8.18%
0.67	190.8E+9	161.3E+9	18.27%	326.8E+6	360.9E+6	-9.44%
0.50	190.5E+9	151.3E+9	25.93%	300.0E+6	336.0E+6	-10.70%

Table 4: 3D Ellipsoidal Void Results

	Elastic Modulus			Yield Stress		
Aspect Ratio	Theoretical	Simulated	Difference	Theoretical	Simulated	Difference
2.00	196.0E+9	198.9E+9	-1.46%	455.5E+6	486.1E+6	-6.30%
1.50	195.9E+9	196.8E+9	-0.46%	446.0E+6	478.0E+6	-6.68%
1.00	195.9E+9	193.0E+9	1.52%	429.3E+6	464.2E+6	-7.52%
0.67	195.8E+9	187.4E+9	4.50%	407.4E+6	446.4E+6	-8.76%
0.50	195.8E+9	182.1E+9	7.50%	387.8E+6	430.5E+6	-9.93%

Table 5: 3D Rectangular Void Results

	Elastic Modulus			Yield Stress		
Aspect Ratio	Theoretical	Simulated	Difference	Theoretical	Simulated	Difference
2.00	191.7E+9	198.2E+9	-3.25%	463.2E+6	489.3E+6	-5.34%
1.50	191.6E+9	196.2E+9	-2.34%	455.4E+6	480.9E+6	-5.31%
1.00	191.3E+9	192.7E+9	-0.72%	441.5E+6	467.5E+6	-5.56%
0.67	191.0E+9	188.1E+9	1.53%	423.4E+6	451.7E+6	-6.27%
0.50	190.6E+9	183.8E+9	3.69%	407.2E+6	438.2E+6	-7.09%

Table 6: 3D Octahedral Void Results

	Elastic Modulus			Yield Stress		
Aspect Ratio	Theoretical	Simulated	Difference	Theoretical	Simulated	Difference
2.00	147.4E+9	197.8E+9	-25.44%	439.2E+6	479.9E+6	-8.48%
1.50	147.1E+9	195.1E+9	-24.61%	426.3E+6	469.9E+6	-9.28%
1.00	146.5E+9	189.5E+9	-22.72%	403.5E+6	451.9E+6	-10.73%
0.67	145.6E+9	181.2E+9	-19.62%	373.5E+6	428.1E+6	-12.75%
0.50	144.8E+9	173.1E+9	-16.35%	346.7E+6	406.5E+6	-14.71%

The results from tables 1-6 clearly show a trend of diverging from the simulation results at lower aspect ratios. This is likely explained by the linear displacement shape functions used to construct the stiffness models – more specifically that the linear displacement assumption is more appropriate where the change in area through the direction of applied force is more gradual, as it is in the high aspect ratio models, than where the area derivative is generally larger as in the low aspect ratio models.

Another cause for this discrepancy is that the stiffness formulation does not account for the non-uniform stress distribution through the solid section caused by significant stress concentration at the nodes, which is increased at lower aspect ratios. This is most obvious when considering the rectangular comparisons as the model is cleanly separated into sections of constant stiffness through the loading axis as this shape is most accurately and simply modelled by the theoretical formulation. Figure 13 shows that the increased stresses through the void section are not simply transferred through the solid section, but also create a moment reaction in the solid section which causes material above and below the void to experience compressive stress. It is due to this response that the computational models experience greater deformations at the same effective stress. This distribution of concentrated stresses is also thought to be the reason that the theoretical models predict a lower yield stress, as the peak stresses are realistically more evenly distributed than conceptualized by the stiffness method.

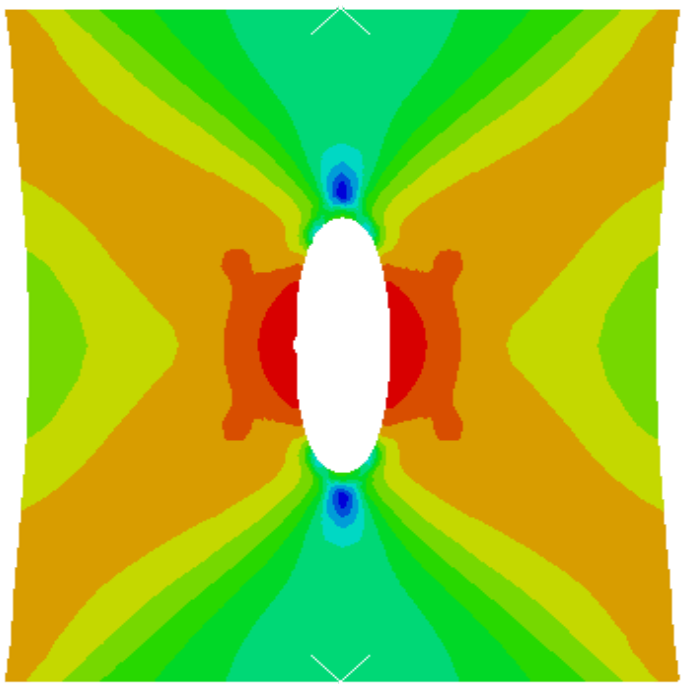

Figure 12: Elliptical Stress Distribution

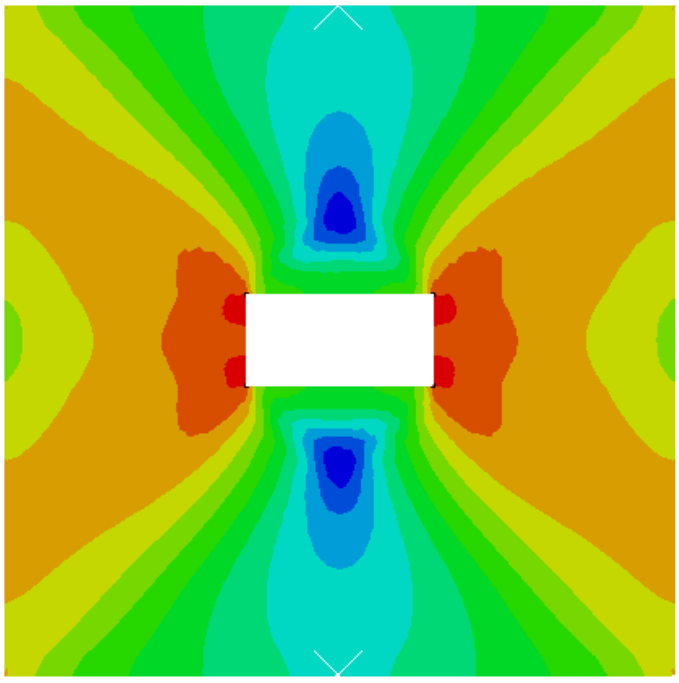

Figure 13: 2D Rectangular Stress Distribution

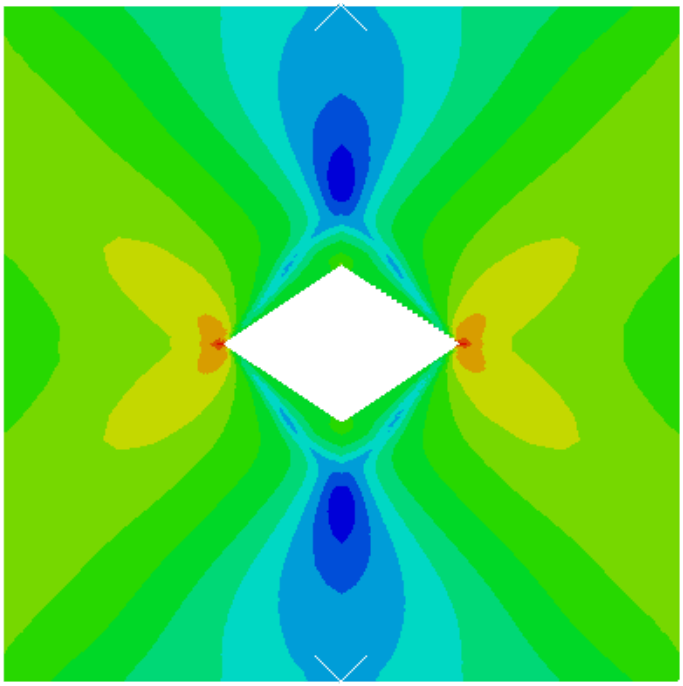

Figure 14: Quadrilateral Stress Distribution

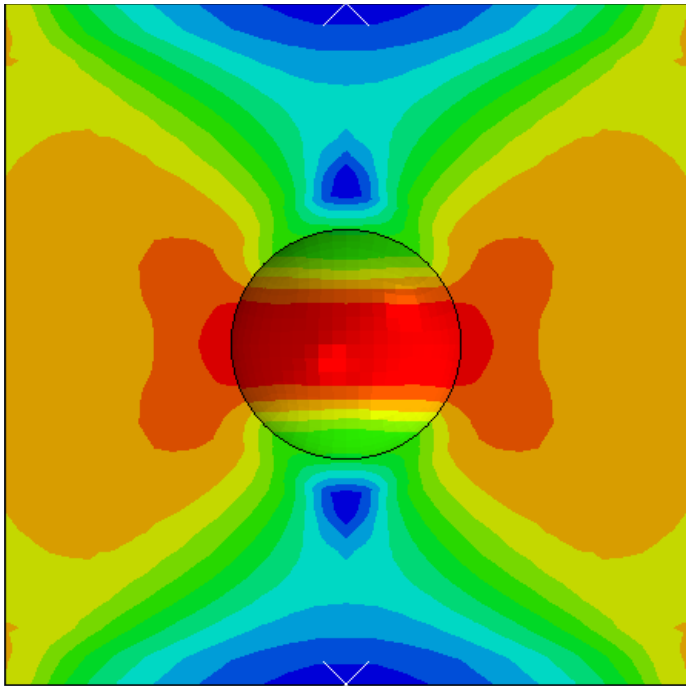

Figure 15: 3D Ellipsoidal Stress Distribution

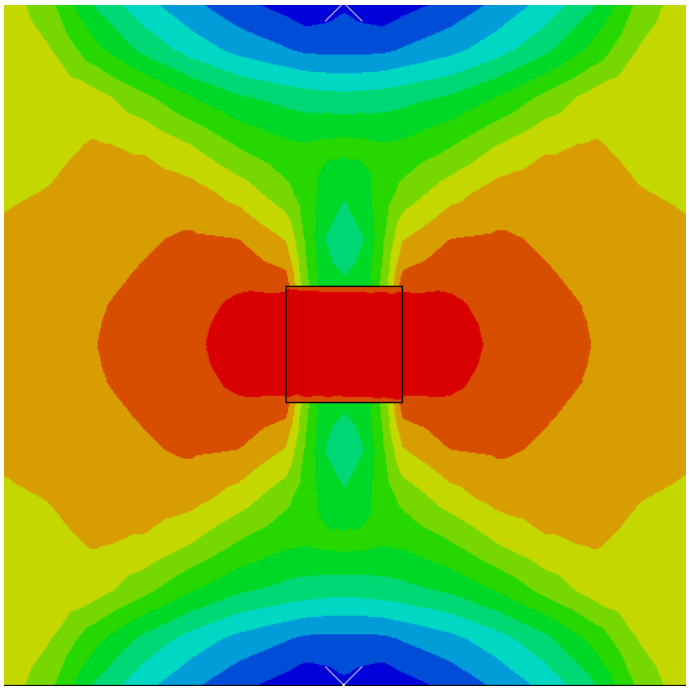

Figure 16: 3D Rectangular Stress Distribution

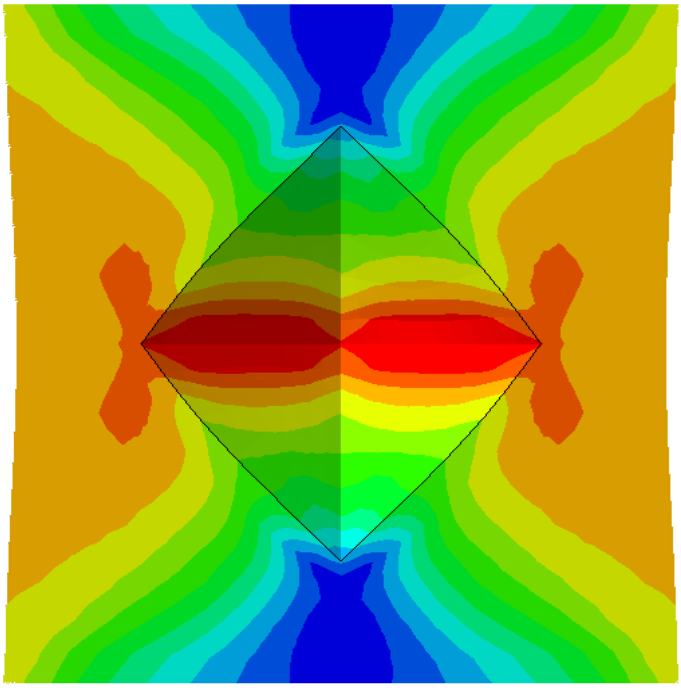

Figure 17: 3D Octahedral Stress Distribution

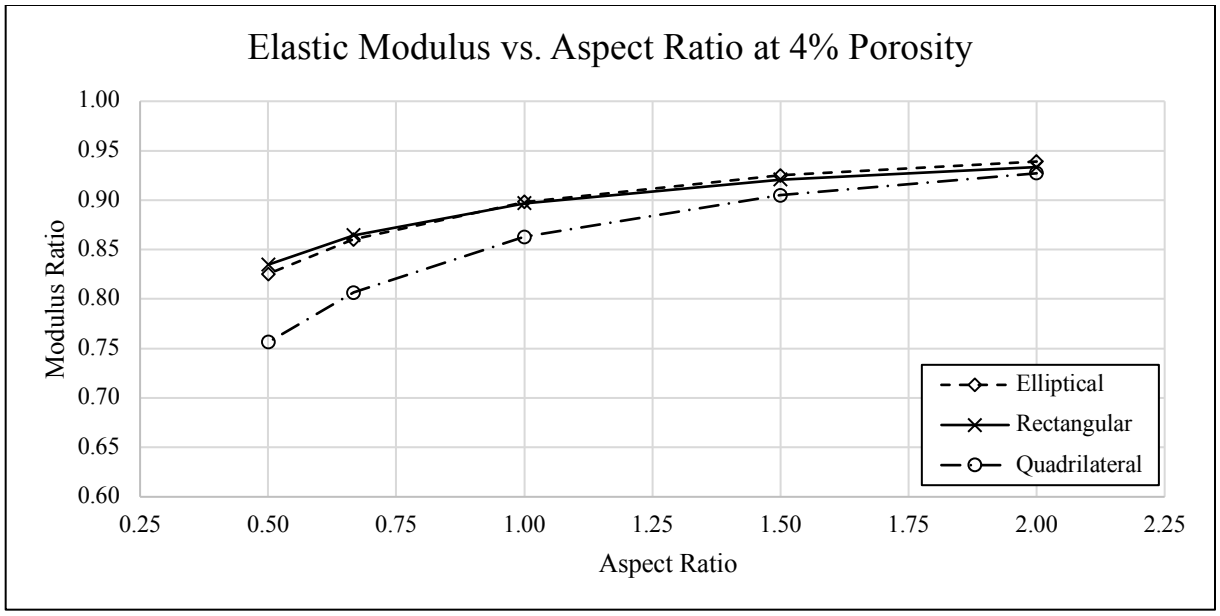

Figure 18: 2D Elastic Modulus vs. Aspect Ratio

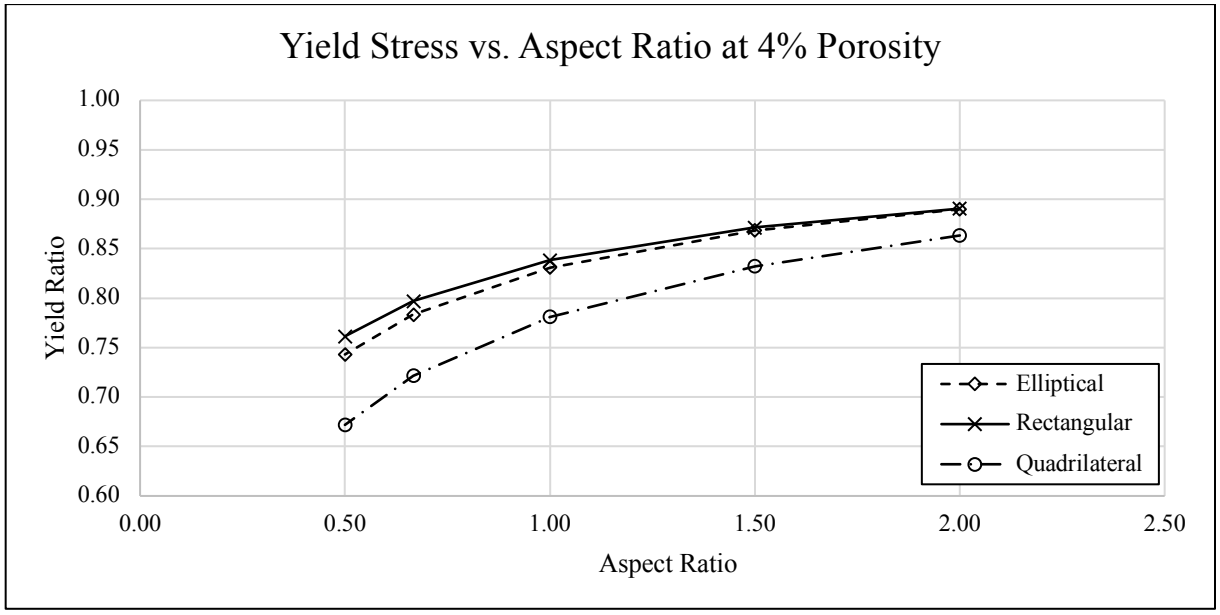

Figure 19: 2D Yield Stress vs. Aspect Ratio

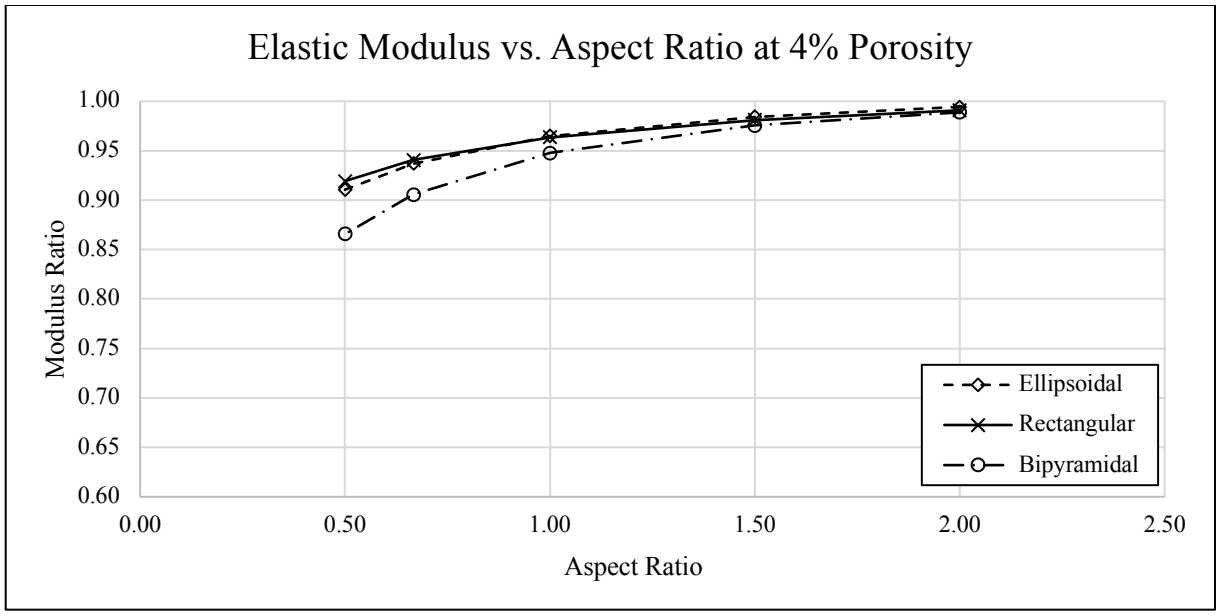

Figure 20: 3D Elastic Modulus vs. Aspect Ratio

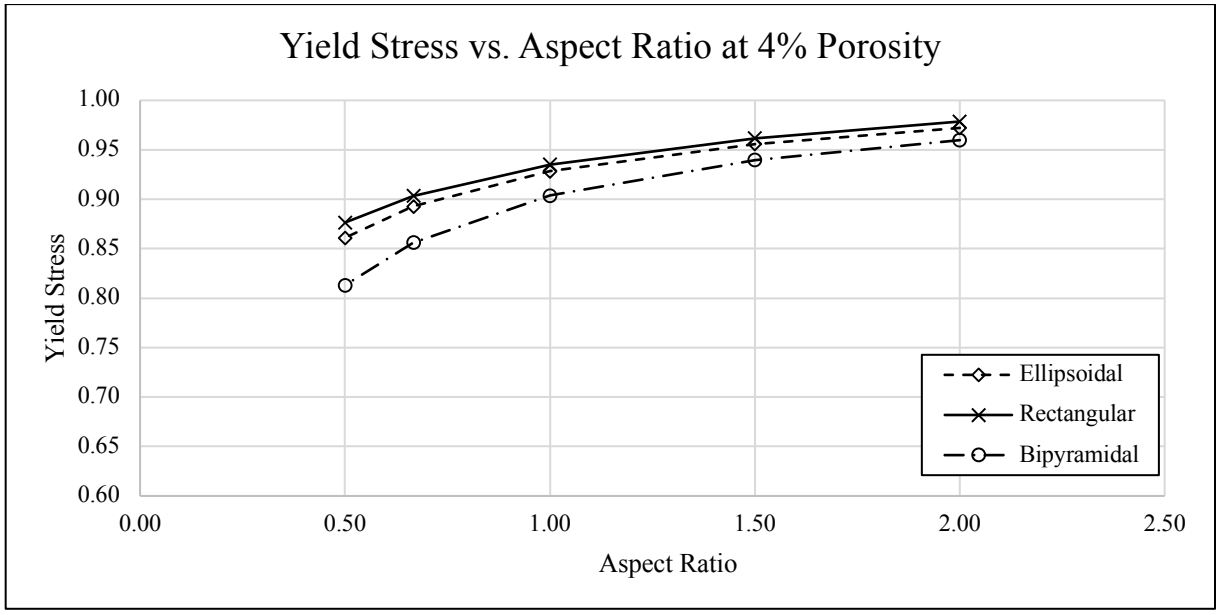

Figure 21: 3D Yield Stress vs. Aspect Ratio

3.4. Conclusions

It is clear from the previous four plots that the aspect ratio and shape characteristics of a void inclusion in a representative volume element have significant influence on the mechanical behavior of the porous material represented by that model. It is therefore imperative that the porous material being investigated through finite element analysis is represented in as realistic a manner as possible. In the case of porous powder-based sintered materials it is necessary to simulate the powder settling and compaction mechanics which occur during the fabrication process in order to accurately replicate the behavior of these materials.

4. Model Generation

The model generation process begins with the generation of particles in the free-state. Given a form of particle size distribution and a user-specified cube side length, spheres of various size are placed at randomly chosen point coordinates within the cube. A placement attempt is accepted if it does not intersect any of the existing spheres. This loop is broken after a specified number of failed placement attempts. A variant of this process is available which prioritizes the placement of large particles and modifies attempted particle sizes in proportion to the number of remaining attempts. The radius equation for this variant is as follows:

$$R_i = R_{min} + (\gamma - R_{min})\left(\frac{i}{n}\right) \tag{4.1}$$

Where γ is the particle radius generated from the size distribution function, i is the current attempt number and n is the maximum number of placement attempts. This processing step effectively reduces computational load and mimics the settling behavior of free particles. The resultant free-state configuration is a densely packed cube of hard spheres where sphere-cube intersections are permitted and sphere-spheres intersections are not.

The fixed-state is achieved iteratively via two processes: compaction and arrangement. The compaction process translates particles proportionally toward the origin, after which the arrangement process evaluates each particle's immediate neighbors and shifts the particle center to the point of least total intersection. This process mimics the physical processes of compaction and settling to achieve a more realistic geometry. The volumetric void fraction is calculated post-arrangement to inform the magnitude of the next compaction. This loop breaks when the absolute difference between the target void fraction and the calculated void fraction dips below a user-defined acceptable error. The error formula is shown in the following equation, where P_t is the target porosity. By default the acceptable error limit is set to 10^{-12}.

$$err = \frac{\left|\left(1 - \frac{V_{voids}}{V_{total}}\right) - P_t\right|}{P_t} \tag{4.2}$$

The compaction process begins with two inputs: the free-state particle configuration and the target void fraction. An initial compaction of 0.95 is applied – that is, the components of each particle are multiplied by the scalar coefficient 0.95, drawing each proportionally towards the origin. This new particle configuration is then arranged to achieve a more natural, settled state. During the arrangement process each particle is investigated for intersecting neighboring particles and consequently translated to the point of least total intersection magnitude (see Figure 24 & Figure 25). The resulting particle can be said to be optimally centered within the local region. The void fraction is calculated once again and used to extrapolate the next compaction coefficient. For an error threshold of $|\text{err}| < 10^{-9}$ this algorithm is observed to reliably achieve the target porosity after fewer than 10 compaction attempts.

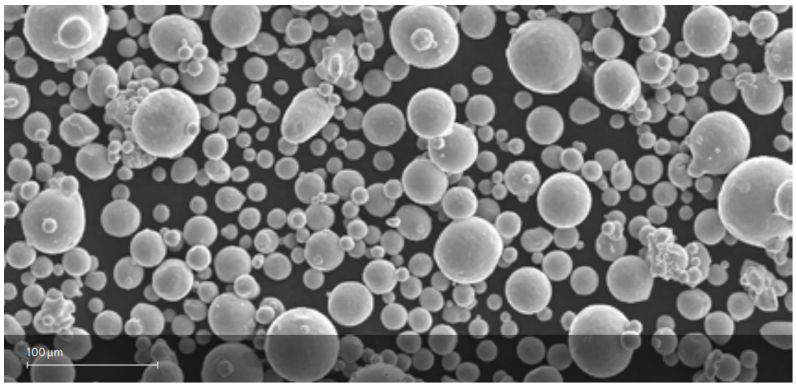

Figure 22: SEM Image of EOS Grade 5 Titanium Powder [31]

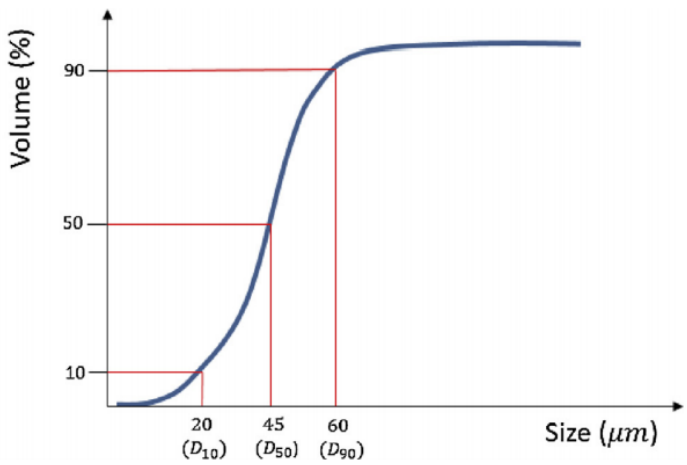

Figure 23: Cumulative Particle Size Distribution [30]

4.1. 2D Porosity Computation

The volume computation implemented here is algebraic, solving both of the noted flaws. In the case of 2D model generation the effective area of a particle is considered to be the segment bounded by all active lines of intersection which contains the center point. This area is computed by geometric decomposition into areas of single, double, and triple inclusion. A lone particle having no intersection with other particles or boundaries consists of one single-included region. A particle intersected by one other particle will have one region of double inclusion, that which belongs to both particles, and one region of single inclusion. The region of double inclusion must be subtracted from the area sum for effective area computation. If this region of double inclusion were to be intersected by a third particle or a boundary then this triple included region will have been counted three times and subtracted three times, and must therefore be added once more. The summation of active regions is governed by the inclusion-exclusion principle of combinatorics. The particular definitions in 2D are summarized in Table 7.

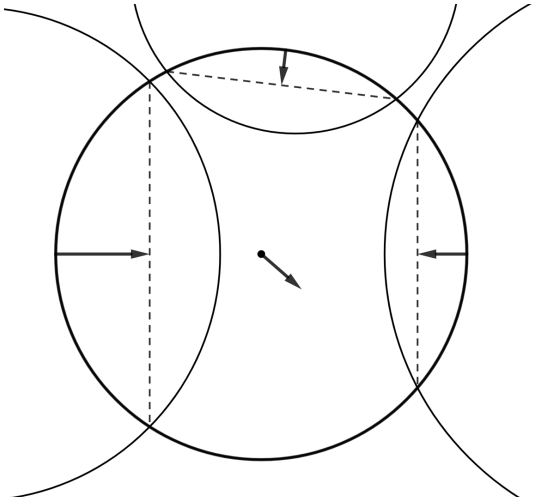

Figure 24: Initial Particle Position

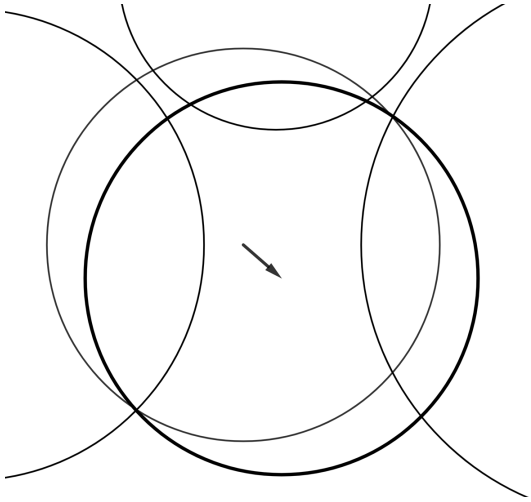

Figure 25: Post-Arrangement Position

Table 7: Inclusion-Exclusion Guide for 2D

Segment Definition	Status
Individual Particle	Included
Particle Exterior To Unit Boundary	Excluded
Particle Exterior To Two Unit Boundaries	Included
Area Common To Two Particles	Excluded
Area Common To Two Particles Exterior To Unit Boundary	Included
Area Common To Three Particles	Included

The area of the region given by a circle-line intersection is found from the equation below.

$$AR_1(D) = \theta r^2 - D\, r \sin\theta \tag{4.3}$$

Where D is the normal distance from the circle center to the line of intersection and $\theta = \text{acos}\,(D\ /\ r)$. In the boundary intersection case depicted in Figure 26 this distance is the length of line AB.

In the case of dual boundary intersection depicted in Figure 26B, we observe that the removal of double-inclusion regions defined by vectors A and B will in turn subtract the region exterior to both boundaries twice. The area of this region must be calculated for re-inclusion. In

this special case where vectors A and B are perpendicular the area of this region is found from the equation below. This equation represents the deconstruction of the intersected regions into a quarter-circle, a rectangle, and one-half of each circular segment.

$$AR_2(\mathrm{A},\mathrm{B}) = \frac{1}{2}\big(AR_1(\mathrm{A}) + AR_1(\mathrm{B})\big) + (\mathrm{A} * \mathrm{B}) - \frac{\pi}{4}r^2 \tag{4.4}$$

Where $AR_2(\mathrm{A},\mathrm{B})$ is the doubly excluded region of the particle from Figure 26B, which is intersected by two perpendicular boundary lines of normal distances A & B from the particle center. The AR_1 terms in this equation represent the single overlap areas from each intersecting boundary line, as derived in Equation 4.3.

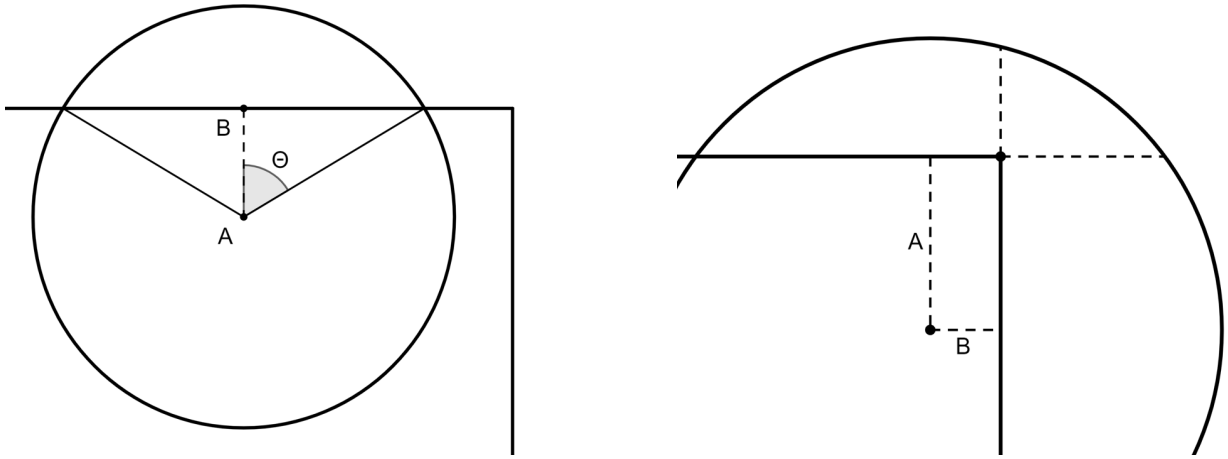

Figure 26: A) Single Boundary Overlap, B) Dual Boundary Overlap

The case of circle-circle intersection is handled as two distinct instances of circle-line intersection where the line is a common chord defined by the pair of points common to both circles. The area to be excluded from each circle is defined by the normal distance from the chord to each circle's center point as seen in Equation 4.5 [32].

$$D = \frac{r_A^2 - r_B^2 + \overline{AB}^2}{2\overline{AB}} \tag{4.5}$$

Where r_A and r_B are the radii of the particle of interest (A) and the intersecting particle (B).

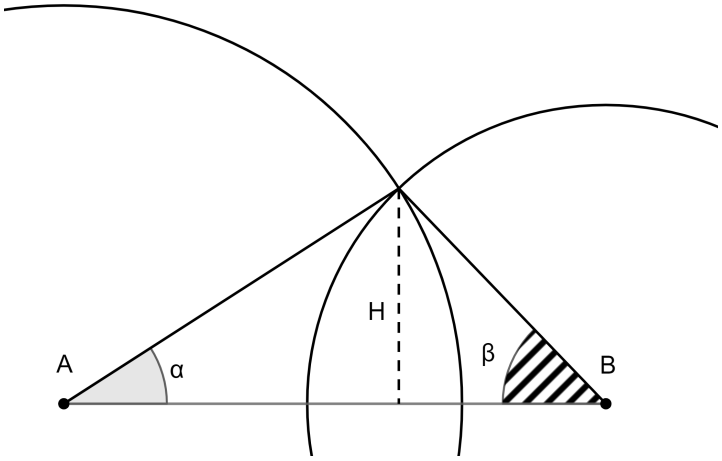

Figure 27: Two-Circle Intersection Properties

The area of circle A exterior to the common chord is determined by substitution of Equation 4.5 into Equation 4.3:

$$AR_{A,B} = \alpha r_A^2 - \left(\frac{r_A^2 - r_B^2 + \overline{AB}^2}{2\overline{AB}}\right) r_A \sin\alpha \tag{4.6}$$

Where

$$\alpha = \operatorname{acos}\left(\frac{r_A^2 - r_B^2 + \overline{AB}^2}{2\overline{AB}\, r_A}\right) \tag{4.7}$$

For the case depicted in Figure 28 where a region common to two circles exceeds the boundary line an inclusion correction must be made to account for the region of triple inclusion. In the figure, the area of circular wedge DFE is constructed from the area of the circular sector defined by α and the areas of triangles ADF and AEF.

$$AR_3 = \frac{1}{2}\alpha r_A^2 - A_{ADF} - A_{AEF} \tag{4.8}$$

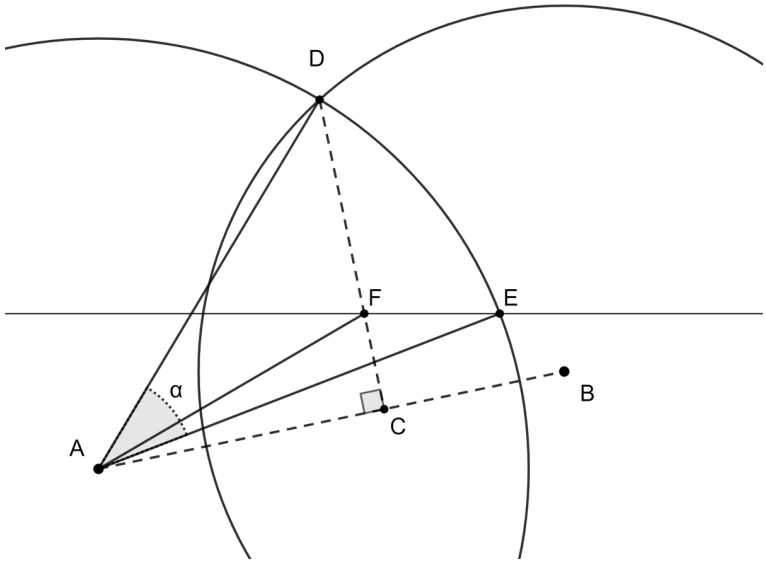

Figure 28: Dual Intersection at Boundary

The area common to three circles is isolated by a similar method of deconstruction. The circular triangle DEF shown in Figure 29 is a triple included region. The population and compaction algorithms are implemented such that a generalized formulation, such as that proposed by Fewell, is excessive – the algorithm will not produce the instances of severe overlap that the generalized form accounts for [32]. The formulation implemented in this application takes advantage of the pre-defined area functions to compute the area of this region accurately. The construction is as follows:

$$AR_{DEF} = AR_{ABC} + \frac{1}{2}(AR_{AB} + AR_{AC} + AR_{BA} + AR_{BC} + AR_{CA} + AR_{CB}) - \frac{1}{2}(\alpha r_A^2 + \beta r_B^2 + \gamma r_C^2) \quad (4.9)$$

Where AR_{ABC} is the area of triangle ABC via Heron's formula [33], and AR_{ij} is the area of circle i exterior to the common chord of circles i and j . Angles $\alpha, \beta,$ and γ are the angles of the vertices of the triangle formed from the particle centers as seen in Figure 29.

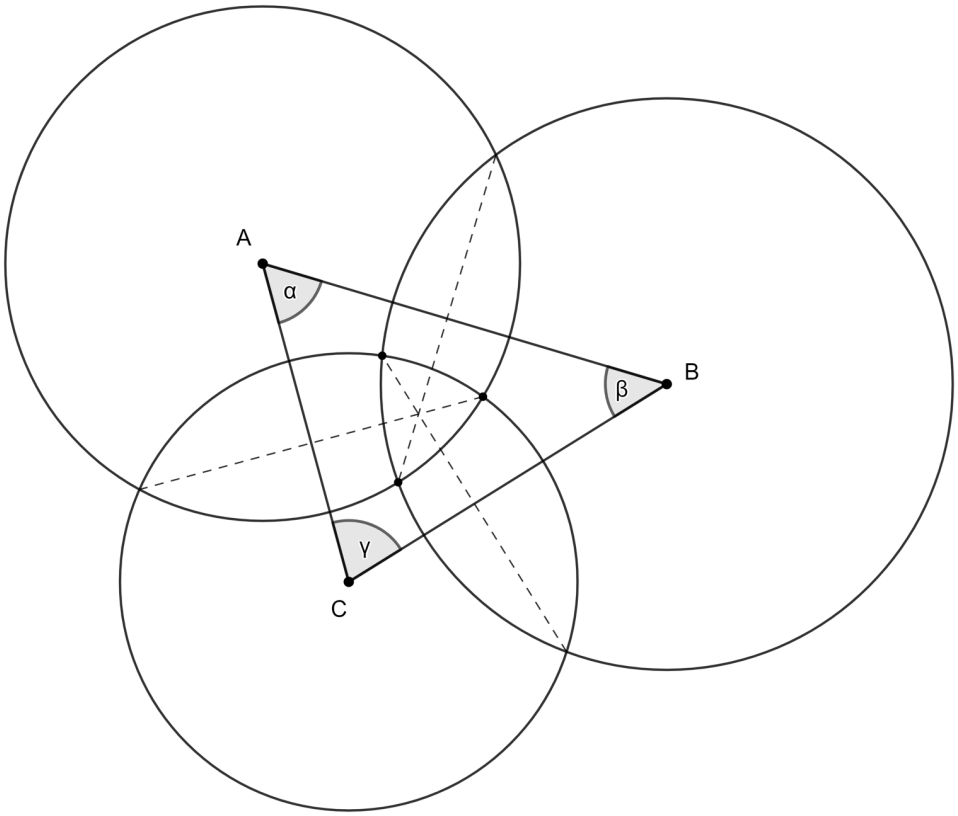

Figure 29: Three-Circle Intersection

4.2. 3D Porosity Computation

The inclusion-exclusion criteria for 3D porosity calculation are listed below.

Table 8: Inclusion-Exclusion Criteria for 3D

Segment Definition	Status
Individual Particle	Included
Volume Exterior To Unit Boundary	Excluded
Volume Exterior To Two Unit Boundaries	Included
Volume Exterior To Three Unit Boundaries	Excluded
Volume Common To Two Particles	Excluded
Volume Common To Two Particles & Exterior To One Boundary	Included
Volume Common To Two Particles & Exterior To Two Boundaries	Excluded
Volume Common To Three Particles	Included
Volume Common To Three Particles & Exterior To One Boundary	Excluded

The volume of each individual particle is combined to produce an initial volume of particles. The two subsequently excluded cases (1 sphere – 1 boundary & 2 spheres) are

functionally identical where the particle of interest is intersected by one plane. Equation 4.5 remains the ideal formula for normal distance, in this case from the sphere center to the plane defined by the common circle for any sphere-sphere intersection [34]. The volume of the spherical cap exterior to one intersecting plane is shown below:

$$V_{cap} = \frac{\pi}{3}(r_A - L)^2(2r_A + L) \tag{4.10}$$

Where L is the normal distance from the intersecting plane to the sphere center. The cases of included intersect volumes such as sphere-plane-plane, sphere-sphere-plane, and triple overlapping spheres are generalizable in the form of one sphere intersected by two intersecting planes. The intersecting planes form a line that intersects the sphere. A projection of the spherical cross-section normal to the intersection line is depicted below.

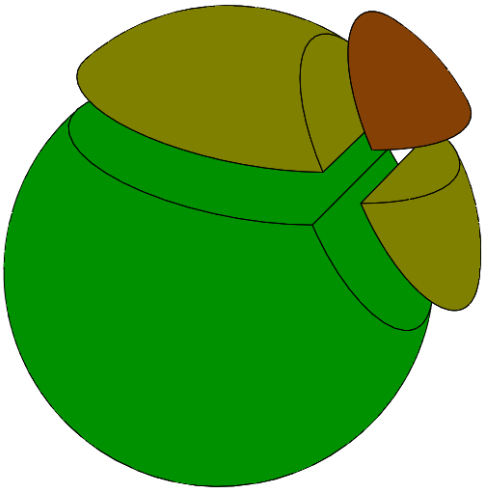

Figure 30: Spherical Segment Exploded View

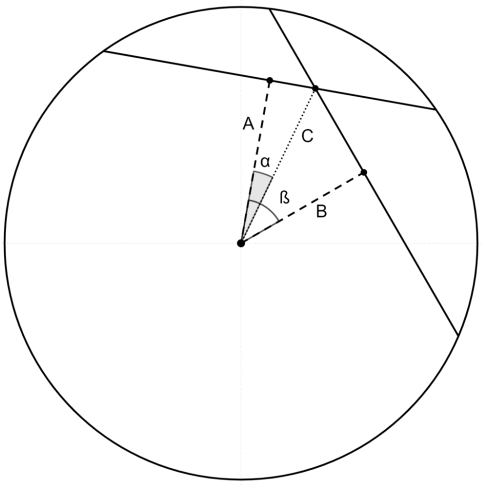

Figure 31: Spherical Segment Cross-Section

Any instance of intersection fitting this characterization can be decomposed into two separately evaluated volumes, where the orange region of Figure 30 is bisected by the plane containing both the intersection line and the sphere center (line “c” in Figure 31). Each of the two

resultant segments take the form depicted in Figure 32 for which the volume is calculated as follows [35].

$$V = \frac{1}{3} r_A^3 \left[\pi - 2 \operatorname{asin}\left(\frac{r_A \cos \alpha}{\sqrt{r_A^2 - H^2}} \right) \right] \tag{4.11}$$

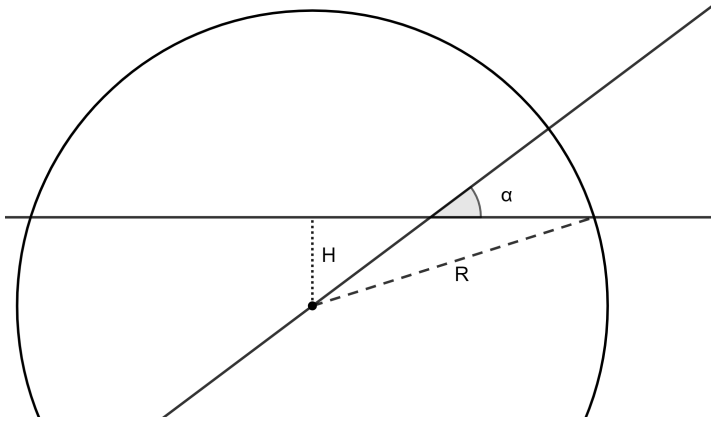

Figure 32: Spherical Wedge Area Derivation

The remaining excluded regions are modelled as the intersection of a sphere and a tetrahedron such that one vertex of the tetrahedron is contained in the sphere as outlined by Bernardeau et al. [36]. In this case three planes intersect at a point within the sphere. The three planes are identified by the normal vector from the plane to the sphere center. This information is sufficient to determine all of the necessary quantities: the dihedral angles of each plane-plane intersection, the coordinates of four intersection points, and the equation of the plane defined by intersection points on the sphere surface. This deconstruction relies on a unique approach to determining the volume of a spherical region which utilizes Girard's theorem. The requisite volume calculations rely on these values to evaluate the following values:

- The area of the spherical triangle ABC given by Girard's theorem
- The volume described by the spherical triangle by integration of the area through the radius
- The volume of the tetrahedron $OABC$, where O is the sphere center (V_{t1})
- The volume of the tetrahedron $XABC$, where X is the triple-plane intersection point (V_{t2})
- The volume of three spherical wedges to correct for the spherical triangle volume approximation (V_{w1}, V_{w2}, V_{w3})

Girard's theorem proposes that a spherical triangle having a spherical excess of $E = a + b + c - \pi$, where $a, b,$ and c are the angles of intersection at each vertex, is related to the surface area of that triangle via the following formula [37].

$$\Delta = R^2 E \tag{4.12}$$

The spherical lines $\overline{AB}$, $\overline{AC}$, and $\overline{BC}$ describe great circular arcs on the sphere surface. As such, the spherical excess E is entirely independent of the radius. Integrating this area through the radius yields the following volume formula.

$$V_{tri} = \int_0^R \rho^2 E \, d\rho = \frac{1}{3} R^3 (a + b + c - \pi) \tag{4.13}$$

The volume V_{tri} of the region depicted in Figure 34 is decomposed into tetrahedron $OABC$ and a triangular spherical cap, each having well defined volumes. The volume of the tetrahedron $XABC$ seen in Figure 35 (orange) is calculated and added to the known volume of the triangular spherical cap (red). The volume of a tetrahedron given four point coordinates is calculated via formulation below.

$$V_{OABC} = \frac{1}{6} \left| \left(\overrightarrow{OA} \times \overrightarrow{OB} \right) \cdot \overrightarrow{OC} \right| \tag{4.14}$$

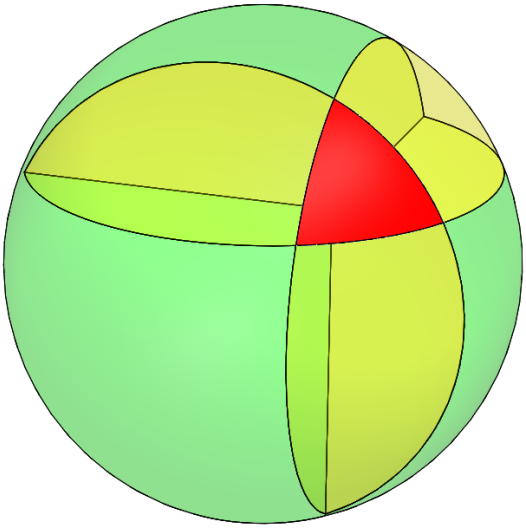

Figure 33: Sphere Intersected by Three Planes

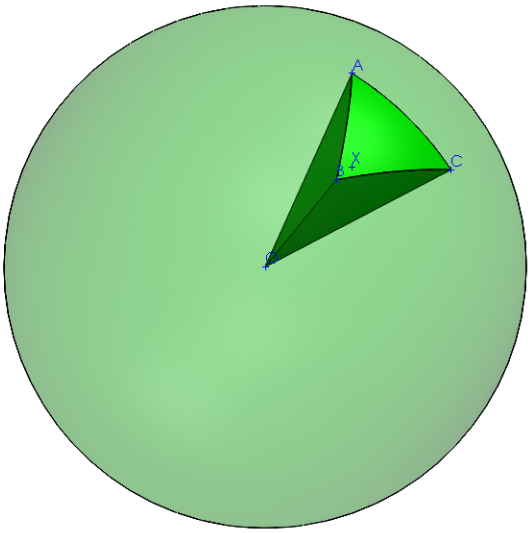

Figure 34: Spherical Triangle Volume

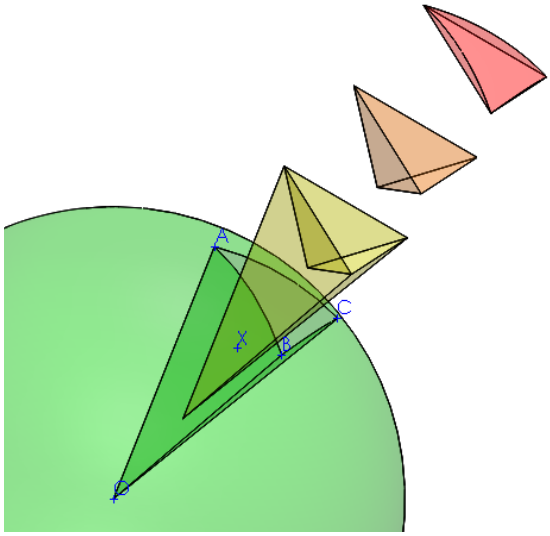

Figure 35: Exploded View

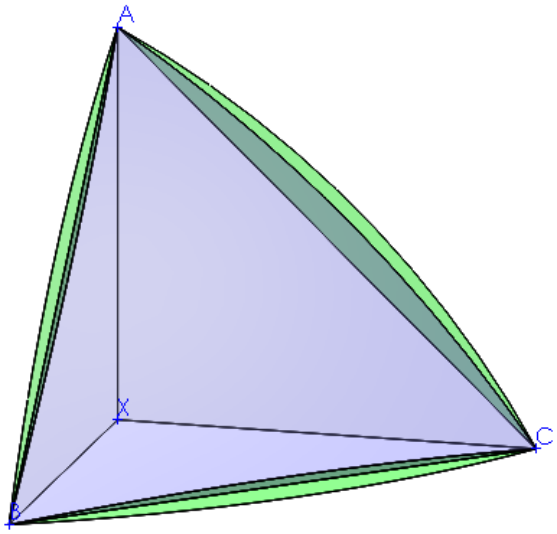

Figure 36: Corrective Spherical Wedges

These regions are combined to form the purple shape seen in Figure 36. The three tetrahedral faces exist on the cutting planes, however, the cap segment is observed to diverge from the cutting planes. Where a tetrahedral face is in the plane XBC the associated cap face will be in the plane OBC due to the decomposition method for V_{tri}. Each of the three remaining wedge volumes are calculated as per Equation 4.11. In this case the height H is the normal distance from plane ABC to point O, and angle α is the dihedral angle formed by, for example, planes OAB and

XAB. Because one plane contains the sphere center point the volume may be evaluated in the special simplified form shown in Figure 32.

The volume computation operations detailed above are implemented in the following manner.

1. **for** all spheres:
2. Compute whole sphere volume
3. **if** sphere-boundary overlap **then**
4. Store normal vector(s) from sphere center to boundary wall(s)
5. **for** remaining spheres ~*i:*
6. **if** sphere-sphere overlap **then**
7. Store normal vector from sphere center to common plane
8. **end for**
9. **for** all intersecting planes:
10. Compute spherical cap volume from plane *q*
11. **for** all intersecting planes ~*q*:
12. **if** plane-plane intersection line in sphere **then**
13. Compute spherical segment volume *q-r*
14. **for** all intersecting planes ~(*q*∨*r):*
15. **if** triple intersection point in sphere **then**
16. Compute triple intersection volume *q-r-s*
17. **end for**
18. **end for**
19. **end for**
20. Combine computed volumes to isolate once-counted volume of sphere *i*
21. **end for**
22. Sum calculated effective sphere volumes

This order ensures that each unique instance of single, double, and triple plane intersection is evaluated a single time.

4.3. Iterative Porosity Solver

Given three known values (boundary length, particle volume, and target porosity) the compaction process will begin to alter particle positions, drawing each sphere proportionally toward the RVE center until the void fraction is determined to be within an acceptably small

margin of the target porosity. This numerical root finding method uses linear extrapolation to suggest compaction levels such that the RVE porosity approaches the target porosity with precision and efficiency.

The mathematical core of the compactor process is a linear equation solver. The solver is initially given an entirely non-intersecting list of particles, a boundary length B_o, and a target porosity P_T. The particle list is fed to a volume calculator function that returns the effective volume of the particles, V_{part}, contained by a unit cube with a negligible wall thickness. The initial porosity is calculated in Equation 4.15.

$$p_o = 1 - \frac{V_{part}}{B_o^3} \tag{4.15}$$

The initial compaction coefficient is $c_o = 1$, indicating that the particle coordinates are unaltered. It can therefore be written that an arbitrary function $f(c_o) = p_o$. If $p_o > P_T$ then a compaction coefficient of 0.95 is attempted. This produces a point for $f(c_1) = p_1$ which is used to predict a new value for c_2. In the generalized form:

$$c_{i+1} = c_i + (c_{i-1} - c_i)\left(\frac{P_T - p_i}{p_{i-1} - p_i}\right) \tag{4.16}$$

This formula extrapolates to produce an estimate for c_n where $f(c_n) = P_T$ using the assumption that this function is approximately linear in the region. For a compaction coefficient $c_n < 1$, the external RVE boundary is equal to the specified boundary length and the internal window is described by internal boundary length B_i below, giving the RVE shell thickness seen in Equation 4.18.

$$B_i = c_n B_o \tag{4.17}$$

$$t_i = \frac{1}{2}(B_o - B_i) = \frac{1}{2}B_o c_n \tag{4.18}$$

A second solid volume, the volume of the shell, is now included in the porosity calculation. The new porosity equation is shown below.

$$V_{void} = B_o^3 p_i = B_o^3 - V_{part} - V_{shell} \tag{4.19}$$

$$p_i = c_i^3 - \frac{V_{part}}{B_o^3} \tag{4.20}$$

4.4. Particle Arrangement

Once a compaction coefficient has been chosen it is applied to the particle coordinates as a scalar multiplier. The new particle coordinates are then passed to an arranger function whose purpose is to compact particles in a manner best resembling the observed characteristics. This function cycles through each particle as in the volume computation function, storing normal vectors of intersecting planes from other particles only – boundary wall intersections are not considered in this module. The normal vectors are processed into a relocation vector:

$$f(\overrightarrow{OA}) = f(x,y,z) = \left(1 - \frac{R}{\sqrt{x^2+y^2+z^2}}\right)\begin{bmatrix} x \\ y \\ z \end{bmatrix} \tag{4.21}$$

In the case where only one intersection plane exists this vector will relocate the particle such that no overlap region exists. For particles with more than one plane of intersection, the vector sum of the relocation vectors will shift the particle into the position of least overlap. The particle's new position replaces its original coordinates so that the next particle rearrangement evaluation considers an up-to-date particle array. The implementation of this arrangement function enhances the computational efficiency of the total volume computation by decreasing instances of complex intersection among particles (3 and 4 particle overlap) and by simplifying the volumetric

decompositions of particle-particle intersections where both particles are centered on a boundary wall or boundary edge. In these special cases, the volume of the spherical cap from a two-sphere intersection belonging to the interior cube is one-half of the cap volume (shared wall) and one-quarter of the cap volume (shared edge). The special cases become increasingly more prevalent at low porosity. The compaction loop follows the order below:

1. Compaction coefficient applied
2. Particle arrangement
3. Porosity computation
4. New compaction coefficient calculated
5. Repeat

A convergence condition is implemented within this loop such that the arrangement step is skipped where the error measurement $|P_t - p_i|$ drops below a specified cut-off. The value of this maximum change threshold must be less than the overall maximum error threshold. From this point, uniform compaction toward the origin is the sole operation performed on the particle coordinates until the target porosity is achieved.

4.4.1. ABAQUS Implementation

Each function described in this document is packaged as a single Python script executable from within the ABAQUS user interface. User inputs such as the dimensionality, population method, particle size distribution, material properties, analysis type, and mesh properties are selected in a graphical window.

4.4.2. Model Generation

The model generation module is handed a particle array and exterior/interior boundary lengths from the compaction function. The model generator begins in the part module, generating a numbered part for each particle in the array with the specified radius. The final part to be created

is the external shell of the RVE. The shell consists of thin walls which envelop the compacted particles to more accurately capture the behavior of the finite element model as an infinite continuous material rather than an isolated unit. Moving to the assembly module, a second loop includes and translates each generated particle to the specified coordinates. The RVE shell is placed in the assembly and merging is performed to produce the final RVE instance. It is at this point that material properties may be applied to the model. The default material model is an elastoplastic formulation, the parameters of which are shown in Table 9.

Table 9: Simulated Material Properties

Material	E (GPa)	$\boldsymbol{\sigma_y}$ (MPa)	$\boldsymbol{\nu}$	$\boldsymbol{\alpha}$	n
CP-Ti	110.0	270.0	0.33	0.13	11.0
Ti-6Al-4V	110.0	380.0	0.37	0.45	24.0
316L SS	190.0	460.0	0.25	0.1	8.5
FSS	80.0	110.0	0.3	0.6	4.7

4.5. Analysis Methods

Two analysis methods, elastic and elastoplastic, are used to extract mechanical behavior from the geometric model. The main script includes modules which function to configure simulations for each analysis method upon completion of the model. In the case of an elastic analysis a linear perturbation load step is used. This method applies a small user-defined strain ($\varepsilon = 0.001$) in a single increment with no time period. The model's linear elastic stiffness is evaluated from the base state, ignoring any and all plastic deformation that may occur [38]. This investigation type is the most rapid and reliable method for computing a structure's elastic stiffness.

The elastoplastic analysis method is intended for investigations of large-deformation behaviours in tension and compression. The nature of compaction behaviour in sintered materials

requires well defined surface self-contact properties. The primary output of this analysis is a homogenized stress-strain relationship capturing both elastic and plastic deformation behavior.

4.5.1. Boundary Conditions

The boundary conditions imposed in both elastic and elastoplastic investigations include rigid top and bottom surfaces. Each node of a rigid surface is tied to a reference node at the center of the face such that these nodes can not move with respect to the reference. A fixed condition is applied to the bottom reference point, restricting the bottom surface completely. A displacement load is generated for the top reference point such that some non-zero uniaxial displacement is applied in the Y-axis during analysis. This condition also restricts rotation of the top surface about the X- and Z-axes. Field output requests are instated to capture reaction force at the bottom reference node and displacement at the top reference node.

5. Simulation Results

5.1. Geometric Accuracy

Models generated by this algorithm are evaluated for their accuracy using mesh-based measurement tools native to the ABAQUS environment. The given measurements are approximations subject to mild discretization error. Sample population comparisons are tabulated below in 2D and 3D at a mean particle radius of one-tenth the unit length.

Table 10: 2D Model Generation Accuracy Comparison

Porosity	Target Area	True Area	% Diff.
20%	80.000	79.944	0.070%
15%	85.000	84.9765	0.028%
10%	90.000	89.949	0.057%
5%	95.000	94.9219	0.082%
4%	96.000	95.894	0.110%
3%	97.000	96.974	0.027%

Table 11: 3D Model Generation Accuracy Comparison

Porosity	Target Volume	True Volume	% Diff.
20%	800.000	799.785	0.027%
15%	850.000	849.155	0.099%
10%	900.000	899.874	0.014%
5%	950.000	949.379	0.065%
4%	960.000	959.409	0.062%
3%	970.000	968.764	0.127%

We observe from Table 10 and Table 11 that the model generation applet reliably generates specimens accurate to the specified target porosity. The area/volume of the final model is found to lie within 0.15% of the target. The area and volume measurements queried by ABAQUS are consistently less than the target values. This discrepancy is explained by the discrete mesh-based method of volume calculation used by the measurement tool. Points are generated on every surface

of the model and connected to form tetrahedra, whose cumulative volume is returned by the query. For any continuous curved surface with a non-zero curvature this will produce some discrepancy inversely proportional to the mesh resolution. In the case of a concave surface the bridging of any two surface points will necessarily fill in a non-existent region, while a convex surface will have regions of its surface cropped out. Since every continuous surface is either flat or convex the volume measurement tool is expected to consistently under estimate the true model volume. The mesh convergence analysis effectively negates the effects of this phenomenon.

The following series depicts the iterative model generation process from generation to completion for a 2D specimen at 5% porosity. The first step shows the particles as they were initially generated. The second step depicts the application of an initial compaction coefficient guess of $c = 0.95$, whose purpose it is to produce a second data point to initialize the iterative process. Steps 3 depicts the final iteration of the compaction process. This particular model had a target area of 95.000 and a measured area of 94.920 for an error of 0.084%.

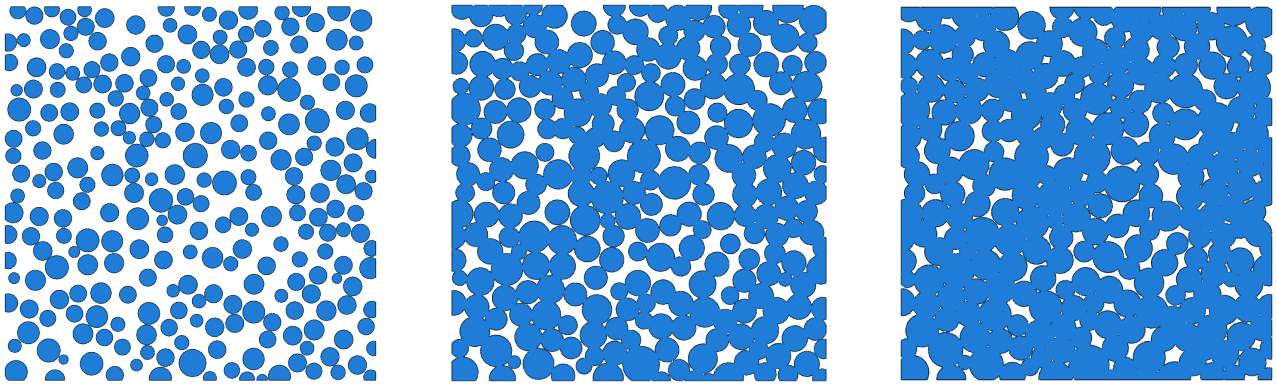

a) b) c)

Figure 37: 2D Compaction Process a) No Compaction b) Initial Compaction c) Final Microstructure

Figure 38 demonstrates the iterative particle compaction method used here to achieve a precise fractional porosity in the microstructure. The error threshold was set to 10^{-12} in this instance.

Figure 39 and Figure 40 depict the particle compaction process in 3D and the porosity convergence plot respectively.

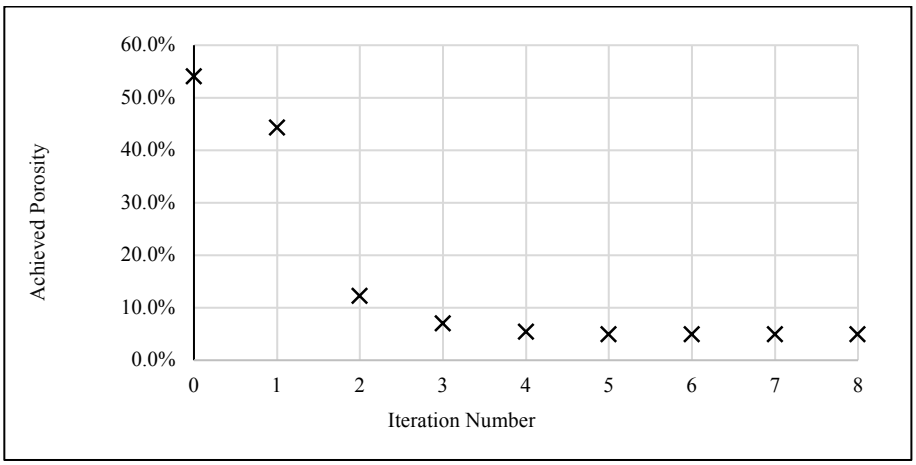

Figure 38: 2D Compaction Plot

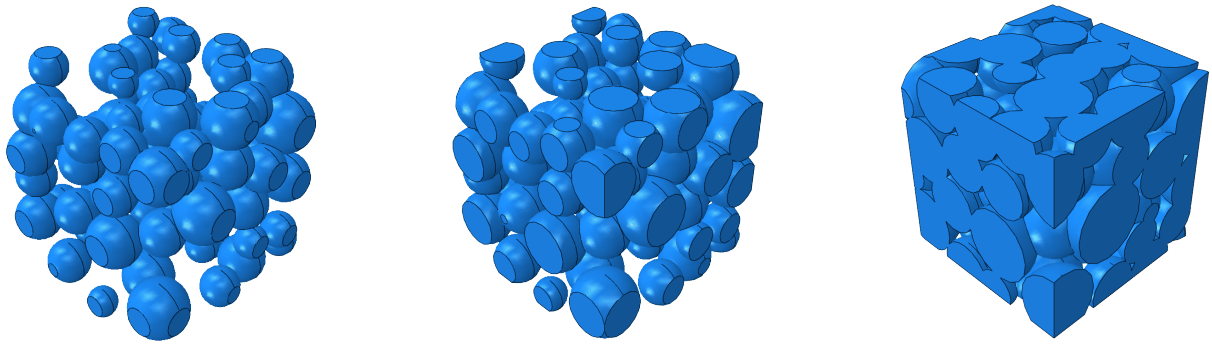

a) b) c)

Figure 39: 3D Compaction Process a) No Compaction b) Initial Compaction c) Final Microstructure

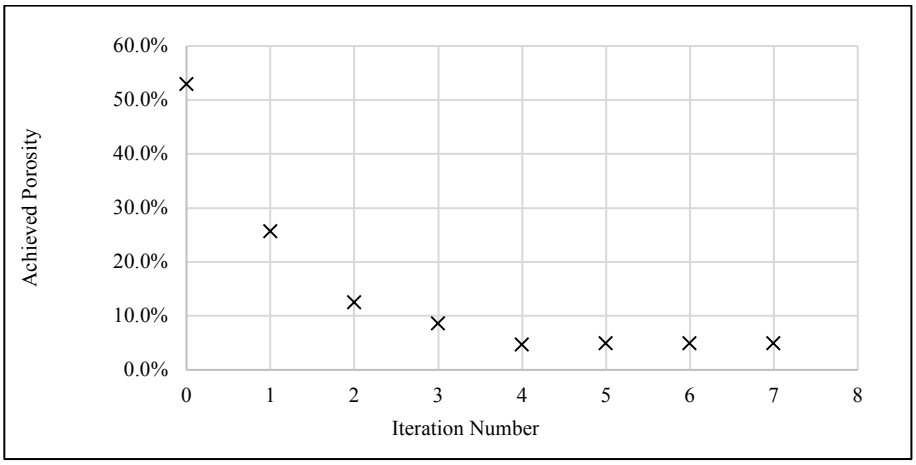

Figure 40: 3D Porosity Iteration Plot

5.2. Mesh Results

Unstructured 2D meshing of a low porosity specimen is shown below at increasing mesh resolution. These are composed of CPS4R and CPS3 mesh elements. The regions of high mesh-density observed in each figure are the result of miniscule voids. The compaction algorithm is designed to reduce the prevalence of tiny voids, however the user may choose to manually fill problematic voids as required. Unstructured 3D specimen meshes are comprised of second order tetrahedral elements.

5.2.1. 2D Simulation Results – Convergence

H-method convergence studies were performed on low- to medium-porosity 2D specimens investigating the effect of porosity on elastic modulus. One such convergence plot is shown in Figure 41 below.

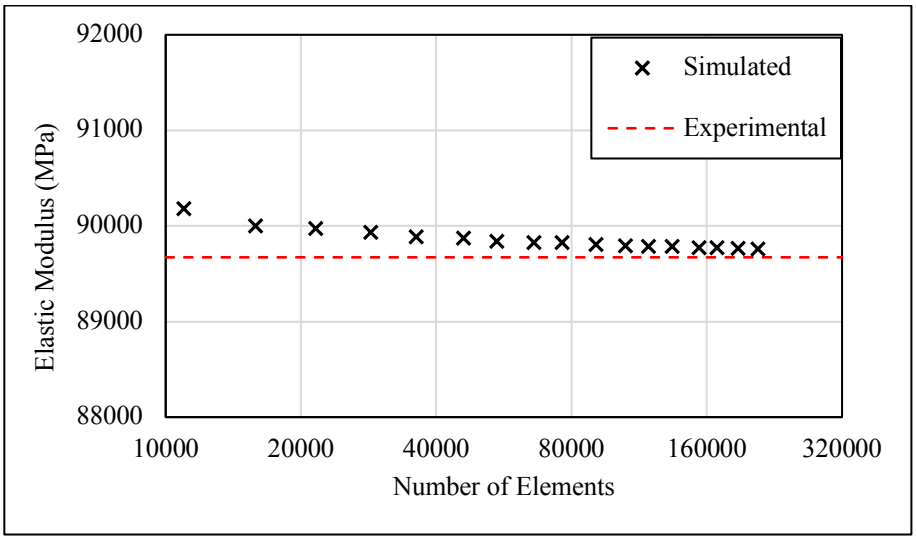

Figure 41: 2D Modulus Convergence Plot (3.6% Porous CP-Ti)

The above data is reconfigured as a percent error in comparison to experimental results and plotted against the total elapsed model generation and simulation time to produce the computational

efficiency plot in Figure 42. These analyses were performed on a HP EliteDesk running Windows 10 with a 3.4 GHz Intel Core i7-6700 processor and 16.0 GB of memory.

5.2.2. 2D Simulation Results – Accuracy

Simulation results for elastic modulus investigations are compared to experimental findings in Table 12. The models used in these simulations were generated with a unit length of 10 and a mean particle radius of 0.5 with a standard deviation of 0.1. A mesh seed was defined with a maximum element length of 0.025, thus achieving a quantity of elements deemed sufficient by the convergence study. The analysis step used was linear perturbation, whereby a very small strain is applied over an arbitrarily small step time assuming linear elastic behavior [38]. We observe that the maximum percent difference in elastic modulus between experimental results and simulation results is 2.83% when comparing titanium and high-strength steel specimens having porosities in the range of 0.9% – 11.7%.

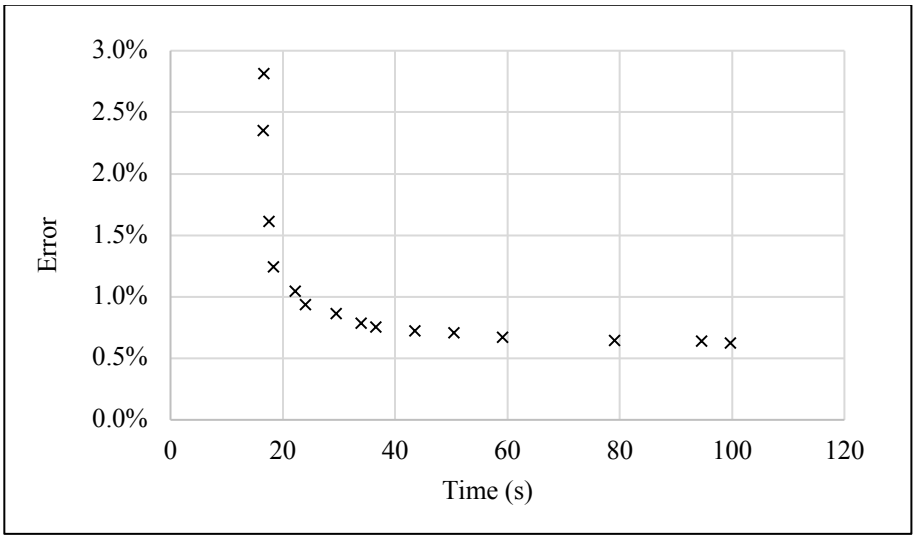

Figure 42: Computational Cost Comparison

5.2.3. 3D Simulation Results – Convergence

We observe from Figure 43 that the elastic modulus converges at approximately 300,000 elements. Lower resolution meshes are inhibited by the very small voids found in the final specimen, which require at least one seed per edge with a growth rate of 1.1 regardless of the global seed size. This growth rate refers to the maximum ratio of adjacent element side lengths in the transition zone from a high resolution to a low resolution mesh region.

5.2.4. 3D Simulation Results – Accuracy

3D simulation results for elastic modulus investigations are shown compared to experimental findings in Table 12. The models used in these simulations were generated with a unit length of 10 and a mean particle radius of 1.0 with a standard deviation of 0.1. A mesh seed was defined with a maximum element length of 0.1, thus achieving a quantity of elements deemed sufficient by the convergence study depicted in Figure 43. The analysis step used was a linear perturbation, as per the 2D simulations. We observe that the maximum percent difference in elastic modulus between experimental results and simulation results is 2.39%.

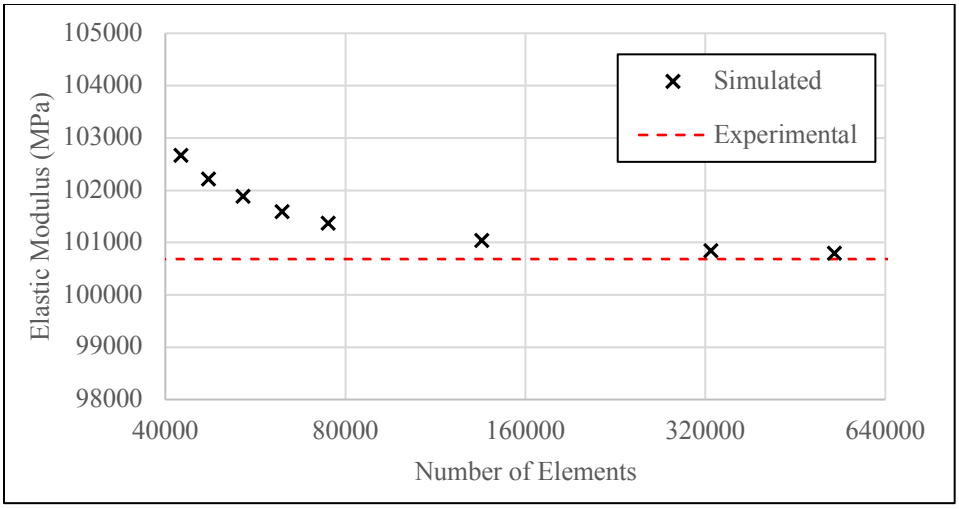

Figure 43: 3D Modulus Convergence Plot

Table 12: Elastic Properties Comparison

Material	Porosity (%)	Elastic Modulus (GPa)	Simulated (GPa)		% Difference	
			2D	3D	2D	3D
CPTi [39]	0.0	110.0	-	-	-	-
	4.5	95.7	95.47	97.45	0.24%	1.83%
	7.8	86.3	84.56	88.361	2.02%	2.39%
Ti-6Al-4V [39]	0.0	110.0	-	-	-	-
	0.9	107.1	105.78	108.012	1.23%	0.85%
	3.5	98.7	98.78	100.361	0.08%	1.68%
HSSS [40]	0.0	144.0	-	-	-	-
	4.0	127.2	124.56	130.17	2.08%	2.33%
	7.0	115.9	112.62	116.72	2.83%	0.71%
HSSS [41]	0.0	170.0	-	-	-	-
	6.5	138.9	136.54	140.24	1.71%	0.95%
	11.7	118.2	116.98	120.33	1.03%	1.80%

5.3. Large Deformation Simulation Results

A series of large deformation analyses were conducted on 2D and 3D specimens in the porosity range of 3.5% - 10.3%. The material properties of the experimental specimens are tabulated below. Given values for offset and hardening exponent refer to the parameters of the deformation plasticity material model which describe the plastic behavior of a fully dense specimen.

In each of the following large deformation analyses the 2D mesh is constructed of free-structured linear tri elements of type CPS3 while 3D meshes use free-structured linear tetrahedral elements type C3D4. In each case the bottom surface is fixed in place while a ramp displacement is applied to the opposite face in a static analysis step with consideration for non-linear geometry effects. A maximum increment time period is specified such that the analysis returns a minimum of 25 data points along the stress-strain curve.

5.3.1. CP-Ti Simulation Results

Figure 46 and Figure 44 depict the simulated mechanical behaviour of porous specimens of commercially pure titanium in comparison to physical test data from Bourcier et al. [39]. These sintered powder-fabricated specimens were loaded in uniaxial tension to failure, with each specimen having a failure strain of $\varepsilon \approx 0.1$.

We observed that, in both trials, the 2D and 3D simulations accurately predict elastic modulus as anticipated. The 3D analyses produce stress-strain behaviour that is highly similar to physical test data up to the ultimate tensile stress. Analysis of 2D models would appear to over-predict the effect of porosity on the tensile yield stress by ~40 MPa in the 4.5% porous study and ~60 MPa in the 7.8% porous model, a percent error of ~14% and ~25% respectively.

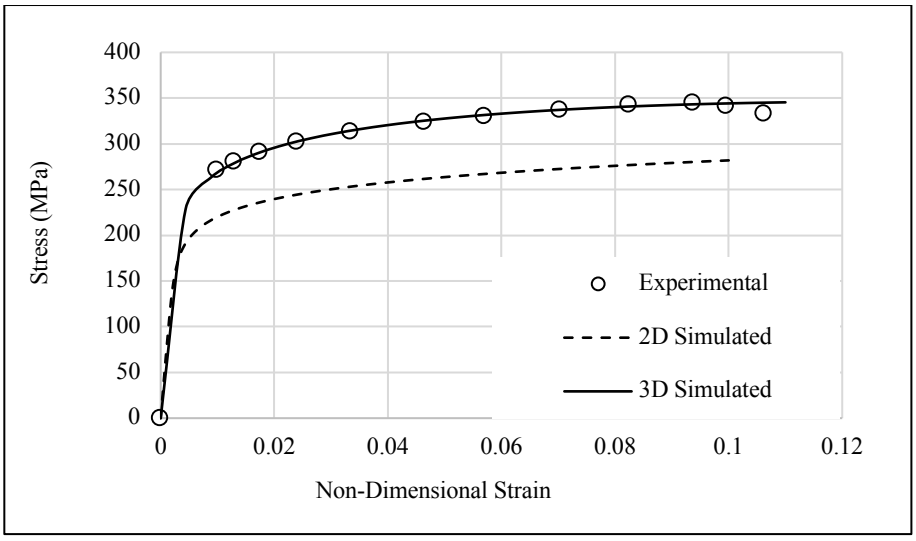

Figure 44: CP-Ti Large Deformation Results – 7.8% Porous

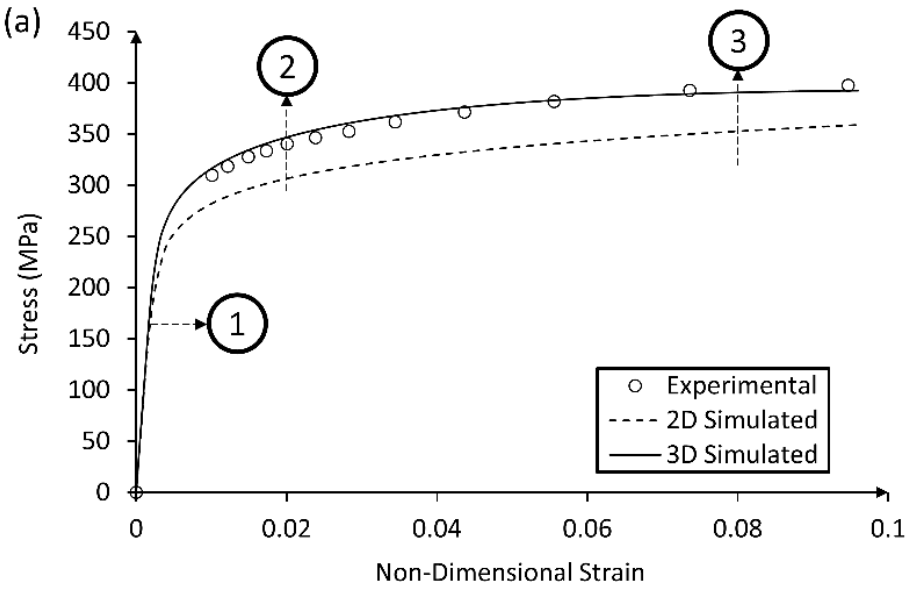

Figure 45: CP-Ti Large Deformation Results – Stress-Strain Plot

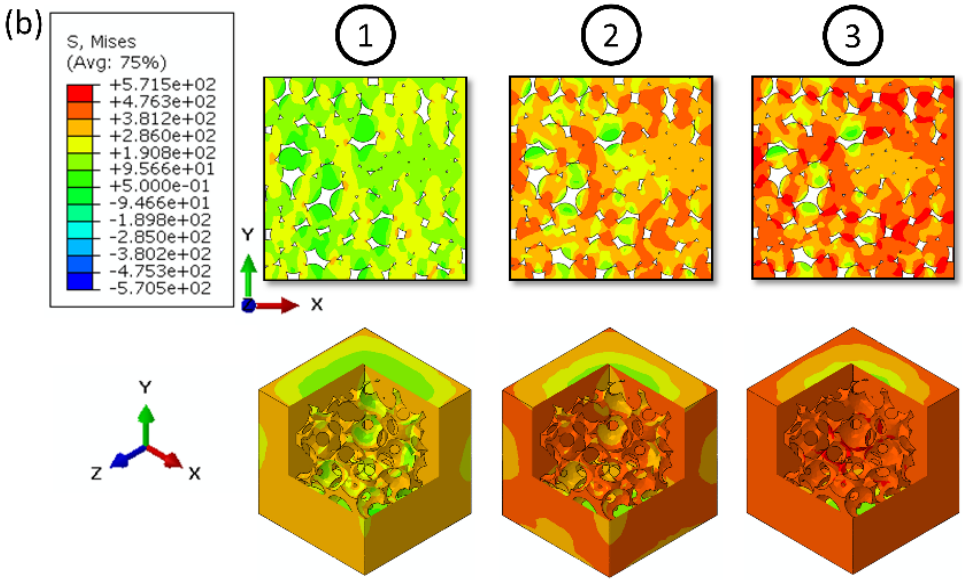

Figure 46: CP-Ti Large Deformation Results – Stress Distribution

5.3.2. Ti-6Al-4V Simulation Results

Figure 47 depicts the simulated mechanical behaviour of a 3.5% porous specimen of grade 5 titanium alloy, once again from Bourcier [39]. This sintered powder-fabricated specimen was loaded to a failure strain of $\varepsilon \approx 0.06$.

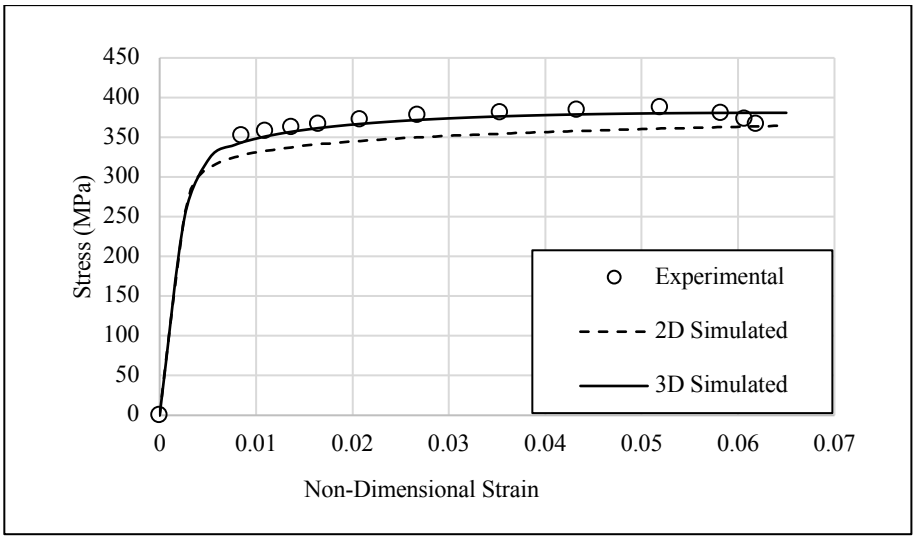

Figure 47: Ti-6Al-4V Large Deformation Results – 3.5% Porous

We observe once again that both 2D and 3D analyses accurately predict elastic behaviour, with 3D providing a good prediction of elastoplastic behaviour and 2D under-predicting yield stress by approximately 8%.

5.3.3. 316L Stainless Steel Simulation Results

Figure 48 and Figure 49 depict the simulated mechanical behaviour of 4.5% and 10.3% porous specimens of 316L stainless steel from Chawla and Deng [42]. Failure strains are recorded as 0.045 and 0.02 respectively.

As we observed in the 4.5% porous CP-Ti comparison, this steel investigation displays an accurate prediction of the elastic properties in both 2D and 3D, under-prediction of yield stress in 2D, and a good prediction of elastoplastic behavior in 3D up to the point of failure. At a porosity

of 10.3%, the 3D model analysis gives an accurate prediction of mechanical behavior throughout the elastoplastic region. The 2D model analysis in this case under predicts both the elastic modulus and the yield stress appreciably.

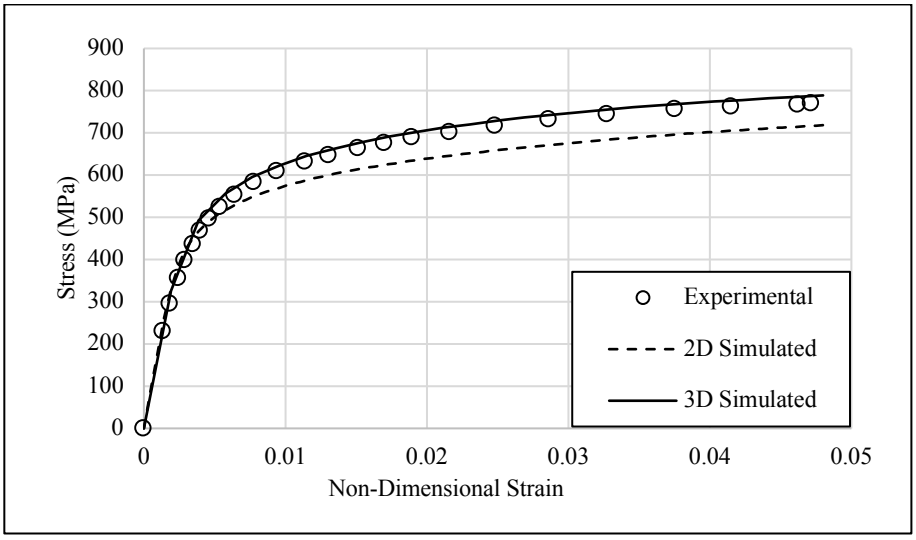

Figure 48: 316L SS Large Deformation Results – 4.5% Porous

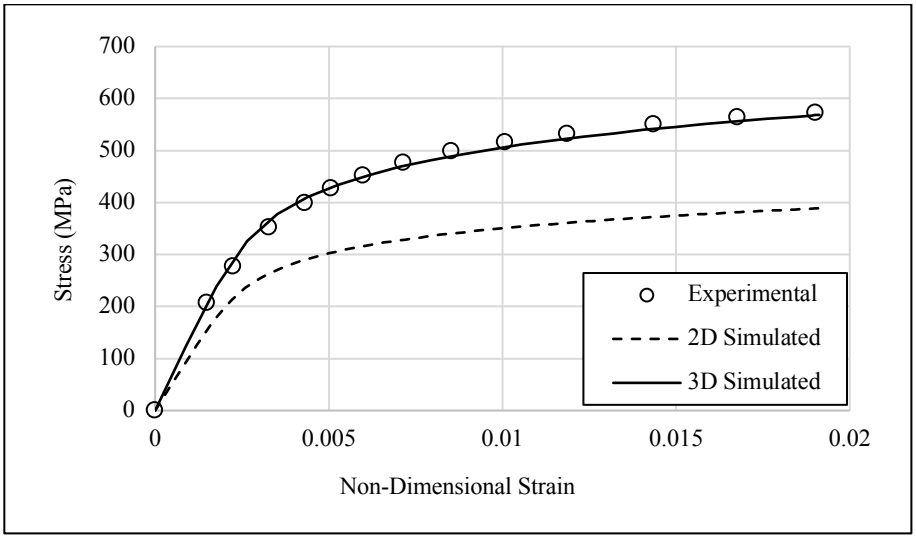

Figure 49: 316L SS Large Deformation Results – 10.3% Porous

5.3.4. Ferrous Sintered Steel Simulation Results

Figure 50 shows the comparison between simulation results and physical test data from the tensile loading of ferrous sintered steel at 9.8% porosity by Bertini et al. [15].

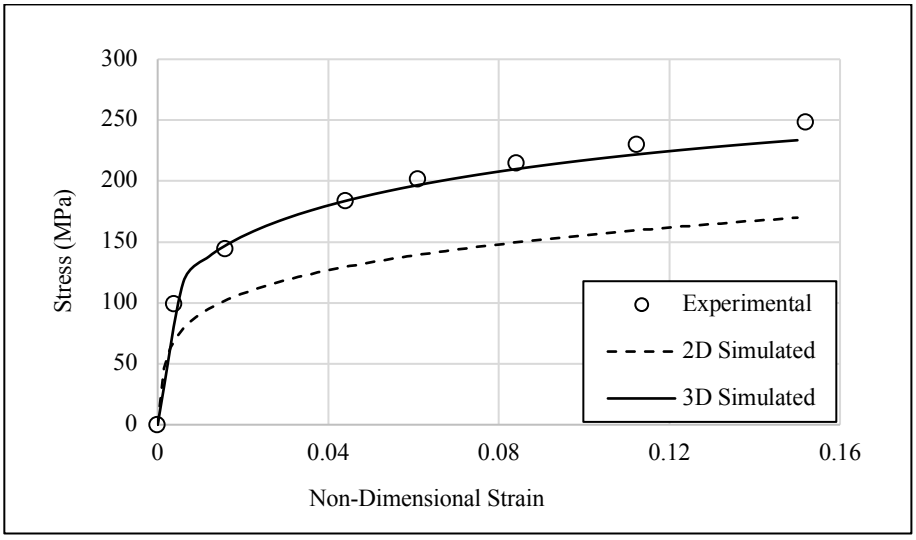

Figure 50: FSS Large Deformation Results – 9.8% Porous

Both modes of model generation appear to capture the elastic properties of the porous specimen, with 3D accurately predicting the plastic strain behaviour up to a strain of ≈ 0.12, and 2D analysis under predicting yield stress by nearly 40%.

5.3.5. Stress Distribution

The stress distributions seen in Figure 51 and Figure 52 correspond to the 4.5% porous sample of 316L stainless steel from 5.3.3. Even at very low strain the effect of void inclusions on the elastic modulus and the yield stress can be well understood. Comparison of the 2D and 3D stress distributions suggests a potential reason for the discrepancies observed in our large deformation simulations. Despite being of identical porosity, the 2D model is more sensitive to the effects of large voids and stress concentrators whereas the 3D model is afforded additional

protection and stability due to the reduced probability of large void clusters occurring in the same plane normal to the direction of applied load. In other words, instances where multiple large voids occur in the same region are less frequent and less severe in 3D than in 2D on account of the additional dimension. A given cross-section of a porous 3D model might display a region of severe weakness due to void inclusions, however, different cross-sections of that same model are unlikely to have large void concentrations in the same plane as the first. Consequently the effects of stress concentrators do not multiply to induce premature yield in 3D the way that we observe in 2D models.

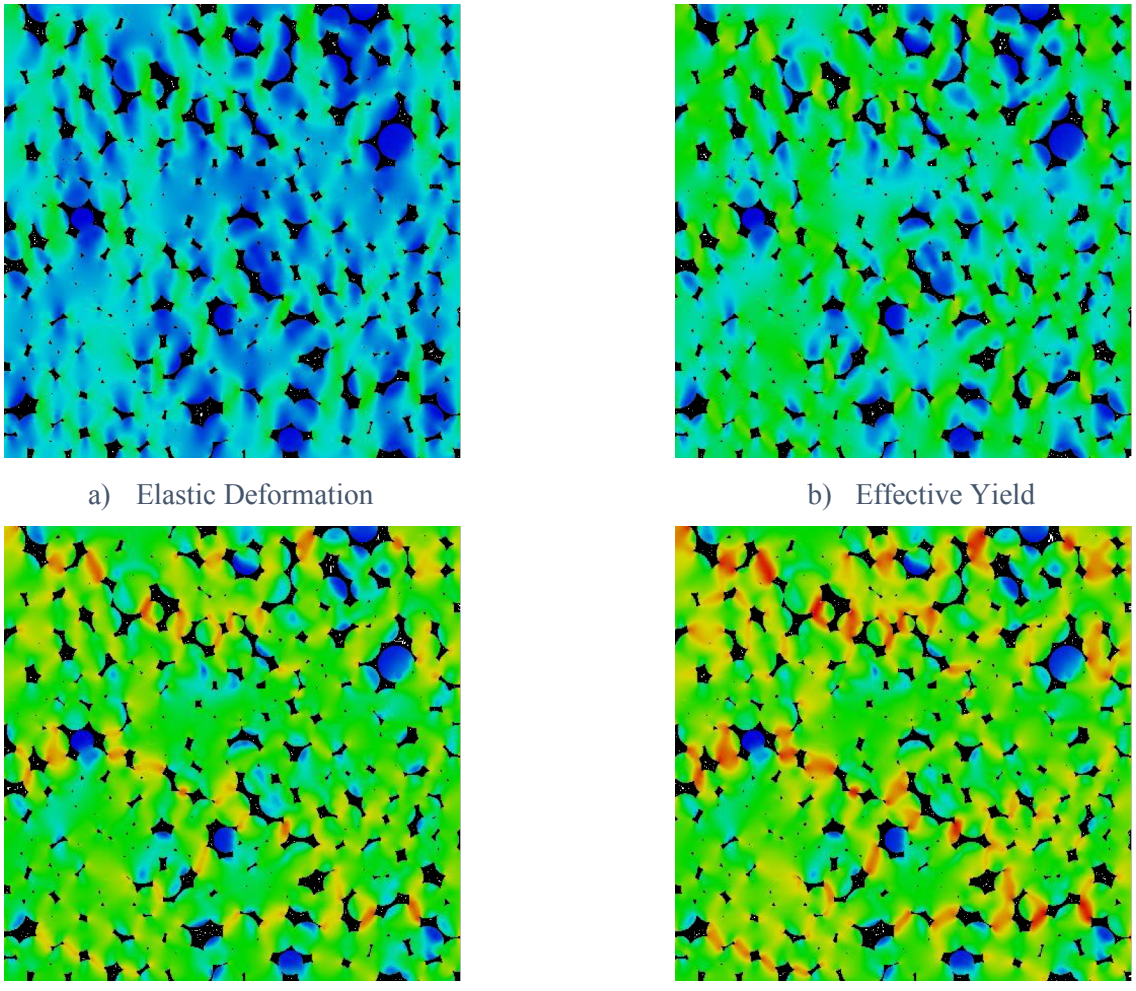

a) Elastic Deformation

b) Effective Yield

c) 2.5% Strain

d) UTS

Figure 51: 2D Large Deformation Stress Distributions

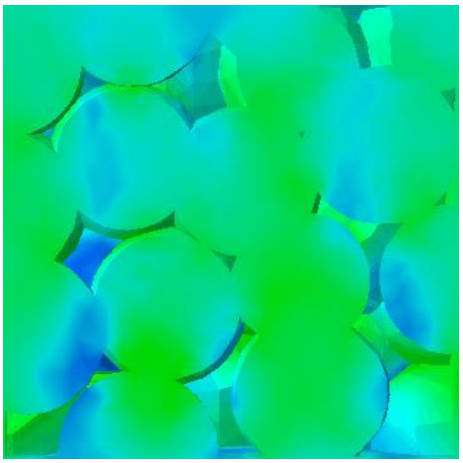

a) Elastic Deformation

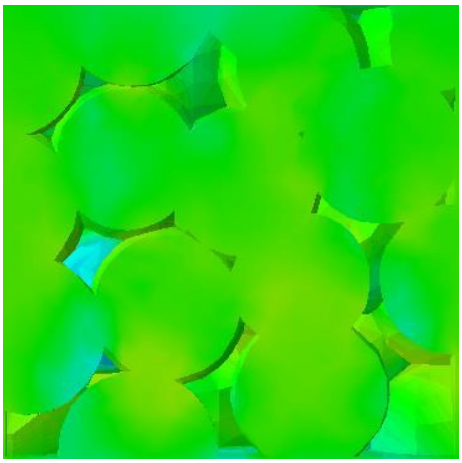

b) Yield Point

c) 2.5% Strain

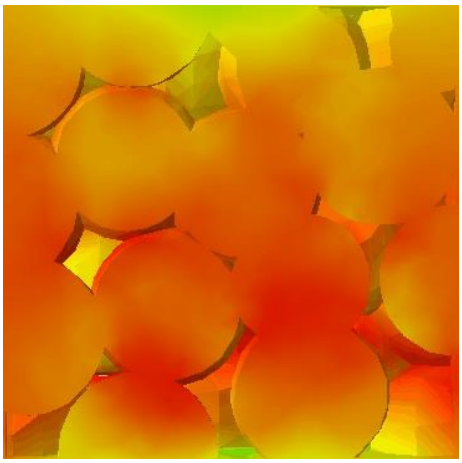

d) UTS

Figure 52: 3D Large Deformation Stress Distributions

5.4. Conclusions

Sections 4 and 5 have shown the development and testing of an algorithm which generates realistic geometric models of powder-based sintered materials. This algorithm relies on two novel processes: one module that rapidly computes the effective volume of a set of intersecting hard spheres and a second process designed to realistically simulate the settling and compaction behavior of spherical particles. Through extensive testing it has been determined that the algorithm quickly, reliably, and accurately produces 2D and 3D representative models from information about the particle size distribution and the porosity level of the final material. Finite element

simulations show that the full elastoplastic behavior of porous sintered materials from physical testing is captured by the corresponding realistic powder-based model.

The particle generation and compaction algorithms produced computational models whose geometric characteristics bear significant resemblance to sintered powder-based porous materials. In particular, the process of iterative particle arrangement captures the phenomenon of free-particle settling and compaction more accurately than any non-iterative random particle placement. The iterative compaction algorithm in concert with the analytical volume calculator have been proven to generate particle-based models of a specified porosity in an automated, precise, and computationally efficient manner. Extensive testing of individual volume evaluation functions suggests that the discrepancies observed between the calculated and the measured model volumes are the result of discretization error inherent in the polygon-based measurement methods.

The tools developed present valuable predictions of mechanical behavior as a function of fractional porosity. Additionally, the anisotropic nature of the representative models allows observations to be made regarding the degree of variance inherent in porous sintered materials. Three dimensional porous RVE models are found to capture large-strain behavior more accurately than two dimensional models, especially at higher porosities. This may be due to the fact that in a pseudo-random system, the weakest cross-sectional line of a 2D model is likely to be weaker than the weakest cross-sectional plane of a 3D model. Three dimensional RVEs should always be used to model the large deformation behavior of porous materials.

The findings of these simulations contribute to our ability to study the effect of void shape, void size, and void fraction on the mechanical properties of porous sintered materials. The model generation application is a powerful tool for the planning and design of devices that stand to benefit from the tailoring of their mechanical behavior.

6. Summary

In the first two sections of this report, published literature, test data, and scans were reviewed to examine the void characteristics of porous materials from various fabrication methods and the effect of porosity and void shape on the mechanical behavior of these materials. It was determined that both the volumetric fractional porosity and void shape characteristics have a significant effect on the elastic and plastic deformation behavior of porous ductile metals. Images of novel additive manufactured particle based metals show that the voids which occur in SLS, SLM, and EBM materials, as well as sintered solids from powder metallurgy, are highly distinct from voids found in non-additive manufactured porous metals. Furthermore, this review of the literature found that the available physical test data from sintered porous specimens is scarce.

Section 3 of this report investigated the effect of porosity and pore shape on the mechanical behavior of porous ductile metals using both a rheological finite element model and computational modelling of the same geometries. Fractional porosity, void shape, and void aspect ratio were used as controlled variables for the in silico experiments. Results from this investigation concluded that the shape and aspect ratio of a void in a ductile material have a significant effect on the elastic modulus, yield, and overall elastoplastic deformation behavior of a porous material. The effectiveness of the analytical finite element modelling of a porous representative volume element as a system of bars with non-uniform cross-sections was tested and it was concluded this model could not replicate the stress distributions observed in the simulated model, especially at lower aspect ratios. This is suggested to be the reason for the discrepancy in results between the two methods.

Section 4 provides a novel method for generating representative volume element models of the powder based sintered geometries of porous sintered solids. The primary challenge of this

work was the development of a system which produces a set of intersecting hard spheres with a particular target volume. The secondary outcome was the realistic representation of particle settling, compaction, and solidification behavior. The model generation algorithm was tested in 2D and 3D for accuracy and mesh convergence. These tests determined that the algorithm produces realistic models of powder based sintered metals rapidly and with high volumetric accuracy. The convergence tests verified that these models are appropriate for use in the finite element simulation of porous materials to study effective material behavior.

Section 5 takes physical test data from porous metal specimens of titanium and steel and builds corresponding models using the novel model generation algorithm. Linear elastic simulations are conducted on these models to determine the effective elastic modulus of each. Large-strain simulations were conducted to gauge the model's prediction of yield and the elastoplastic deformation behavior in general. It was concluded from these comparisons that the procedurally generated 3D models are highly effective at predicting the small and large strain behavior of porous sintered metals.

6.1. Future Work

The model generation system presented here has been proven to have significant potential pertaining to the further investigation of the behavior of porous sintered solids. Given the novelty of these materials and the consequent scarcity of physical test data, this model generation algorithm which has been validated for use in tension can be extended to study the compressive, fatigue, and damage characteristics of these porous materials. The existence of a realistic representative model of the powder-based solids in a finite element environment also facilitates the further study of pore collapse mechanisms on the compressive plastic behavior of these materials. Ultimately data from these simulations might contribute to the development of homogenized analytical models of the

elastoplastic behavior of porous materials parameterized by porosity and void shape characteristics.

References

[1] J.A. Choren, S.M. Heinrich, M.B. Silver-Thorn, Young's modulus and volume porosity relationships for additive manufacturing applications, J. Mater. Sci. 48 (2013) 5103–5112. https://doi.org/10.1007/s10853-013-7237-5.

[2] A. Sola, A. Nouri, Microstructural porosity in additive manufacturing: The formation and detection of pores in metal parts fabricated by powder bed fusion, J. Adv. Manuf. Process. 1 (2019) 1–21. https://doi.org/10.1002/amp2.10021.

[3] S.M. Gaytan, L.E. Murr, F. Medina, E. Martinez, M.I. Lopez, R.B. Wicker, Advanced metal powder based manufacturing of complex components by electron beam melting, Mater. Technol. 24 (2009) 180–190. https://doi.org/10.1179/106678509X12475882446133.

[4] M. Agarwala, D. Bourell, J. Beaman, H. Marcus, J. Barlow, Direct selective laser sintering of metals, Rapid Prototyp. J. 1 (1995) 26–36. https://doi.org/10.1108/13552549510078113.

[5] S.F.S. Shirazi, S. Gharehkhani, M. Mehrali, H. Yarmand, H.S.C. Metselaar, N. Adib Kadri, N.A.A. Osman, A review on powder-based additive manufacturing for tissue engineering: Selective laser sintering and inkjet 3D printing, Sci. Technol. Adv. Mater. 16 (2015) 1–20. https://doi.org/10.1088/1468-6996/16/3/033502.

[6] J.P. Kruth, Material Incress Manufacturing by Rapid Prototyping Techniques, CIRP Ann. - Manuf. Technol. 40 (1991) 603–614. https://doi.org/10.1016/S0007-8506(07)61136-6.

[7] W.E. Frazier, Metal additive manufacturing: A review, J. Mater. Eng. Perform. 23 (2014) 1917–1928. https://doi.org/10.1007/s11665-014-0958-z.

[8] K. Subramanian, N. Vail, J. Barlow, H. Marcus, Selective laser sintering of alumina with polymer binders, Rapid Prototyp. J. 1 (1995) 24–35. https://doi.org/10.1108/13552549510086844.

[9] J. Sedlak, D. Rican, M. Piska, L. Rozkosny, Study of materials produced by powder metallurgy using classical and modern additive laser technology, Procedia Eng. 100 (2015) 1232–1241. https://doi.org/10.1016/j.proeng.2015.01.488.

[10] G.D. Cremer, Powder Metallurgy, U.S. Patent 2355954, (1942) 3–5. https://patents.google.com/patent/US2355954A/en?oq=2355954.

[11] A. Iebba, Maurizio; Astarita, Antonello; Mistretta, Daniela; Colonna, Ivano; Liberini, Mariacira; Scherillo, Fabio; Pirozzi, Carmine; Borrelli, Rosario; Franchitti, Stefania; Squillace, Influence of Powder Characteristics on Formation of Porosity in Additive Manufacturing of Ti-6Al-4V Components, J. Mater. Eng. Perform. 26 (2017) 4138–4147. https://doi.org/10.1007/s11665-017-2796-2.

[12] S.E. Brika, M. Letenneur, C.A. Dion, V. Brailovski, Influence of particle morphology and size distribution on the powder flowability and laser powder bed fusion manufacturability of Ti-6Al-4V alloy, Addit. Manuf. 31 (2020) 100929. https://doi.org/10.1016/j.addma.2019.100929.

[13] H.H. Hausner, The effect of porosity on the structure of sinterered metals, J. Japan Soc. Powder Powder Metall. 7 (1960) 58–72. https://doi.org/10.2497/jjspm.7.58.

[14] K. Yamaguchi, N. Takakura, S. Imatani, Materials Processing Technology, Adv. Mater. Res. 418–420 (2012) 1–6.

[15] L. Bertini, V. Fontanari, G. Straffelini, Tensile and bending behavior of sintered alloys: Experimental results and modeling, J. Eng. Mater. Technol. Trans. ASME. 120 (1998) 248–255. https://doi.org/10.1115/1.2812351.

[16] C.T. Sun, R.S. Vaidya, Prediction of composite properties from a representative volume

element, Compos. Sci. Technol. 56 (1996) 171–179. https://doi.org/10.1016/0266-3538(95)00141-7.
[17] M. Ostoja-Starzewski, Material spatial randomness: From statistical to representative volume element, Probabilistic Eng. Mech. 21 (2006) 112–132. https://doi.org/10.1016/j.probengmech.2005.07.007.
[18] S. Roy, N. Khutia, D. Das, M. Das, V.K. Balla, A. Bandyopadhyay, A.R. Chowdhury, Understanding compressive deformation behavior of porous Ti using finite element analysis, Mater. Sci. Eng. C. 64 (2016) 436–443. https://doi.org/10.1016/j.msec.2016.03.066.
[19] W.M. Harris, W.K.S. Chiu, Determining the representative volume element size for three-dimensional microstructural material characterization. Part 1: Predictive models, J. Power Sources. 282 (2015) 552–561. https://doi.org/10.1016/j.jpowsour.2015.02.035.
[20] P. Kumar, J. Farah, Influence of processing parameters on properties of Inconel 718, Mater. Lett. 252 (2019) 256–259.
[21] Z. Zhang, X.X. Yao, P. Ge, Journal Pre-proof, 2019.
[22] Y. Yang, Lei; Yan, Chunze; Han, Changjun; Chen, Peng; Yang, Shoufeng; Shi, Mechanical response of a triply periodic minimal surface cellular structures manufactured by selective laser melting, Int. J. Mech. Sci. 148 (2018) 149–157. https://doi.org/10.1016/j.ijmecsci.2018.08.039.
[23] M. Smith, Z. Guan, W.J. Cantwell, Finite element modelling of the compressive response of lattice structures manufactured using the selective laser melting technique, Int. J. Mech. Sci. 67 (2013) 28–41. https://doi.org/10.1016/j.ijmecsci.2012.12.004.
[24] H.H. Cho, Y. Cho, H.N. Han, Finite element analysis for mechanical response of Ti foams with regular structure obtained by selective laser melting, Acta Mater. 97 (2015) 199–206. https://doi.org/10.1016/j.actamat.2015.07.003.
[25] P.R. Woodmansee, A finite element analysis of porosity effect on materials, (1989).
[26] H. Shen, L.C. Brinson, Finite element modeling of porous titanium, Int. J. Solids Struct. 44 (2007) 320–335. https://doi.org/10.1016/j.ijsolstr.2006.04.020.
[27] H. Richter, Mote3D: An open-source toolbox for modelling periodic random particulate microstructures, Model. Simul. Mater. Sci. Eng. 25 (2017). https://doi.org/10.1088/1361-651X/aa629a.
[28] A.Y. Elruby, S. Nakhla, Extending the Ramberg–Osgood Relationship to Account for Metal Porosity, Metall. Mater. Trans. A Phys. Metall. Mater. Sci. 50 (2019) 3121–3131. https://doi.org/10.1007/s11661-019-05236-7.
[29] K. Krishnan, W.S. Slaughter, R.J. McAfee, I. Nettleship, A representative volume element for the densification of powders, J. Am. Ceram. Soc. 89 (2006) 2311–2313. https://doi.org/10.1111/j.1551-2916.2006.00983.x.
[30] J.H. Tan, W.L.E. Wong, K.W. Dalgarno, An overview of powder granulometry on feedstock and part performance in the selective laser melting process, Addit. Manuf. 18 (2017) 228–255. https://doi.org/10.1016/j.addma.2017.10.011.
[31] EOS GmbH, EOS Titanium Ti64 - Material data sheet, (2017). https://www.eos.info/material-m.
[32] M. Fewell, Area of common overlap of three circles, DSTO Def. Sci. Technol. Organ. (2006) 30. http://www.dtic.mil/docs/citations/ADA463920.
[33] W. Dunham, Heron's Formula for Triangular Area, in: Journey through Genius Gt. Theorems Math., Wiley, New York, 1990: pp. 113–132.

[34] W.F. Kern, J.R. Bland, Solid Mensuration with Proofs, Wiley, New York, 1948.
[35] K.D. Gibson, H.A. Scheraga, Volume of the intersection of three spheres of unequal size. A simplified formula, J. Phys. Chem. 91 (1987) 4121–4122. https://doi.org/10.1021/j100299a035.
[36] F. Bernardeau, R. Van de Weygaert, A new method for accurate estimation of velocity field statistics, Mon. Not. R. Astron. Soc. 279 (1996) 693–711. https://doi.org/10.1093/mnras/279.2.693.
[37] E.W. Weisstein, Spherical Triangle, Mathworld - A Wolfram Web Resour. (n.d.). https://mathworld.wolfram.com/SphericalTriangle.html (accessed May 6, 2020).
[38] Dassault Systemes, ABAQUS 6.14 Documentation, (2014).
[39] R.J. Bourcier, D.A. Koss, R.E. Smelser, O. Richmond, The influence of porosity on the deformation and fracture of alloys, Acta Metall. 34 (1986) 2443–2453. https://doi.org/10.1016/0001-6160(86)90147-1.
[40] H. D'Armas, L. Llanes, J. Peñafiel, J. Bas, M. Anglada, Tempering effects on the tensile response and fatigue life behavior of a sinter-hardened steel, Mater. Sci. Eng. A. 277 (2000) 291–296. https://doi.org/10.1016/s0921-5093(99)00533-x.
[41] G. Straffelini, Impact fracture toughness of porous iron and high-strength steels, Metall. Mater. Trans. A Phys. Metall. Mater. Sci. 31 (2000) 1443–1451. https://doi.org/10.1007/s11661-000-0262-4.
[42] N. Chawla, X. Deng, Microstructure and mechanical behavior of porous sintered steels, Mater. Sci. Eng. A. 390 (2005) 98–112. https://doi.org/10.1016/j.msea.2004.08.046.